

Matrix mechanics and water permeation regulate extracellular vesicle transport

Stephen Lenzini, Raymond Bargi, Gina Chung and Jae-Won Shin[✉]*

Cells release extracellular vesicles (EVs) to communicate over long distances, which requires EVs to traverse the extracellular matrix (ECM). However, given that the size of EVs is usually larger than the mesh size of the ECM, it is not clear how they can travel through the dense ECM. Here we show that, in contrast to synthetic nanoparticles, EVs readily transport through nanoporous ECM. Using engineered hydrogels, we demonstrate that the mechanical properties of the matrix regulate anomalous EV transport under confinement. Matrix stress relaxation allows EVs to overcome the confinement, and a higher crosslinking density facilitates a fluctuating transport motion through the polymer mesh, which leads to free diffusion and fast transport. Furthermore, water permeation through aquaporin-1 mediates the EV deformability, which further supports EV transport in hydrogels and a decellularized matrix. Our results provide evidence for the nature of EV transport within confined environments and demonstrate an unexpected dependence on matrix mechanics and water permeation.

EVs are cell-derived particles found in the ECM¹ and described as ranging from 50 to 500 nm in diameter². However, the ECM has a range of mechanical properties and often features average mesh sizes smaller than those of the EVs³ (Fig. 1a).

To evaluate the extent to which EVs transport through the interstitial ECM, we engineered EVs from mouse mesenchymal stromal cells (MSCs) to contain the EV marker CD63 fused with Katushka2S (K2S, a far-red fluorescent protein⁴) to visualize them after passive loading by incubation in a decellularized matrix from lung tissue. MSCs were chosen as the source of EVs because in vivo they are often present in interstitial regions surrounded by matrix⁵. The expression of CD63–K2S in EVs (K2S–EVs) did not alter their expected size distribution (diameter (d) \approx 50–150 nm) (Supplementary Fig. 1a). Multiphoton second harmonic imaging analysis showed that the EVs were distributed throughout the collagen fibres within the matrix (Fig. 1b). Despite a nanoscale mean porosity (Supplementary Fig. 1b,c) of the matrix, \sim 50% of the loaded CD63–K2S–EVs were released from the matrix within \sim 24.7 h (Fig. 1c,d), which suggests that EVs readily transport through naturally derived nanoporous matrices.

A decellularized matrix exhibited a complex shear modulus magnitude G^* of \sim 750 Pa with a loss tangent (viscous modulus/elastic modulus, G''/G') of \sim 0.15 (Fig. 2a and Supplementary Fig. 2a), and a stress relaxation behaviour ($t_{1/2} \approx$ 15 s) (Fig. 2b). To determine whether the matrix mechanics mediates the EV transport, we engineered alginate-based hydrogels with a range of mechanical properties known to be present in tissues⁶. Importantly, alginate-based hydrogels are bio-inert, non-degradable and exhibit homogeneous nanoporous structures⁷, which makes them ideal to model ECM without the influence of biochemical or degrading interactions. Hydrogels can be crosslinked physically through divalent cations or

covalently through click chemistry, and G^* is tunable for both (Fig. 2c (left) and Supplementary Fig. 2b). Physical crosslinking leads to stress relaxing hydrogels and covalent crosslinking leads to elastic hydrogels, as indicated by the loss tangent (Fig. 2c (right)) and stress relaxation times (Fig. 2d)⁸. We consider $G^* \approx$ 500 Pa as ‘soft’ and $G^* \approx$ 3,000 Pa as ‘stiff’. Alginate-based hydrogels are nanoporous, like the decellularized matrix (Supplementary Fig. 2c), regardless of the crosslinking density or type. This is consistent with the egg-box model of crosslinking between alginate chains⁹, in which increased crosslinking is not expected to dramatically alter the mesh size. As expected, after dextran–FITC (hydrodynamic radius \sim 15 nm (ref. ¹⁰)) molecules were encapsulated in the hydrogels, most released completely within 24 hours (Fig. 2e). In contrast, a minimal release was observed for polystyrene nanoparticles (NPs; $d \approx$ 80–100 nm) (Supplementary Fig. 2d). As for decellularized tissue, some EVs released from the hydrogels; however, surprisingly, EV release was greater from stress relaxing hydrogels with a higher G^* . This effect occurred for EVs from other cells (Supplementary Fig. 2e), which suggests its generalizability across cell type. Liposomes with a similar size (Supplementary Fig. 2f) and lipid content as those of EVs¹¹ did not exhibit a higher release from stress relaxing hydrogels with a higher G^* (Supplementary Fig. 2g). Hydrogels did not undergo degradation or loss of mass over the tested time period (Supplementary Fig. 3a), which confirms the independence of degradation. Importantly, this observation is independent of Ca^{2+} , as treatment with ionomycin or EGTA did not affect the release (Supplementary Fig. 3b,c). To test whether the EV release is mechanosensitive in a more natural ECM composition, an interpenetrating network hydrogel of alginate and collagen-I polymers was fabricated¹² in which the hydrogel G^* was tunable independent of the collagen-I concentration (Supplementary Fig. 3d). Although EV release from the interpenetrating network was generally lower, depending on the collagen concentration, the release remains mechanosensitive (Supplementary Fig. 3e).

To study whether the EV release from engineered hydrogels corresponds to individual EV transport, we developed a three-dimensional (3D) particle-tracking approach that utilized high-speed 3D microscopy with deconvolution to visualize (Fig. 3a and Supplementary Videos) and calculate the mean square displacement (MSD) of the CD63–K2S–EVs over time in different environments. Particles were tracked immediately after hydrogel formation to capture the initial behaviours possibly affected by hydrogel swelling. Data were collected every $\Delta t = 0.267$ s over a total time $T \approx$ 8 s. Next, data were ensemble-averaged over numerous tracks and fit to the power law form¹³:

$$\langle \text{MSD}(t) \rangle = K_a t^\alpha \quad (1)$$

to calculate an effective ensemble exponent α and coefficient K_a . The effective diffusion coefficient:

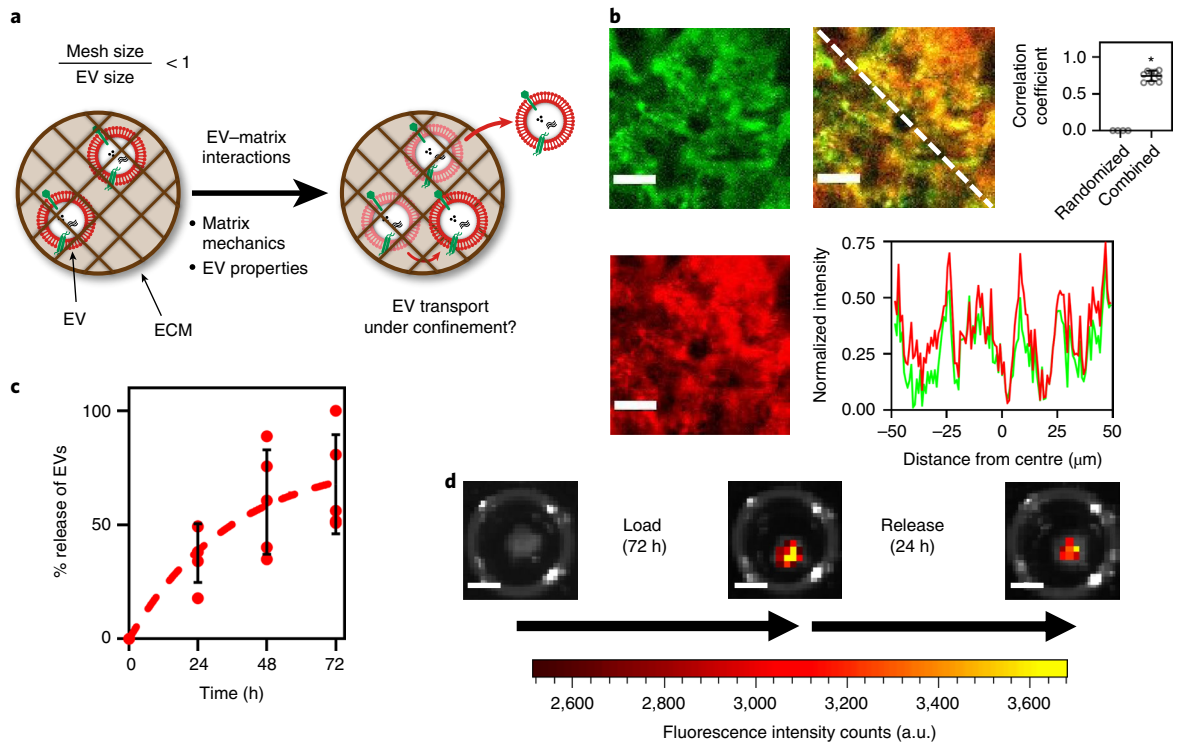


Fig. 1 | EVs transport within decellularized lung tissue. **a**, EVs exist within ECMs, where often the mesh size is smaller than the size of EVs. Mechanisms and dependencies directing their potential transport under confinement are unclear. **b**, Representative images of collagen (top left), K2S-EVs (bottom left) and combined (top middle) of decellularized lung tissue with EVs passively loaded, imaged using second harmonic multiphoton microscopy. Scale bars, 15 μm. A pixel intensity chart (bottom right) drawn along the dotted line in the combined image demonstrates that EVs existed along fibres as the K2S pixel intensity correlates strongly with the collagen pixel intensity. The mean Pearson's correlation coefficient (top right) is reported for $N=9$ regions of interest analysed across 3 pairs of background-subtracted images. * $P < 10^{-15}$ via an unpaired two-tailed t -test. Error bars denote the s.e.m. **c**, Mean % of EV released from the decellularized lung tissue over time with $t_{1/2} = 24.7$ h. $N=5$ tissue slices across 3 independent experiments. **d**, Representative images of EV load (after 72 h) and release (after 24 h) in decellularized lung tissue. a.u., arbitrary units. Scale bars, 2 mm. Error bars denote the s.d.

$$D_{\tau} = \text{MSD}(\tau) / 6\tau \quad (2)$$

was calculated for each track over each interval $\tau = 4\Delta t \approx 1.06$ s (ref. ¹⁴) to give:

$$D_{1.06s} = \text{MSD}(\tau = 1.06 \text{ s}) / 6(1.06 \text{ s}) \quad (3)$$

Multiple values for $D_{1.06s}(\tau)$ were obtained for a single track for each interval τ and averaged to obtain a single $D_{1.06s}$ for each track (Methods). We validated our method by measuring the transport of NPs in glycerol solutions with different solution viscosities and thus different expected transport speeds. NPs in these solutions show an α of ~ 1 (Supplementary Fig. 4a,b), which indicates diffusive transport. Furthermore, they exhibited diffusion coefficients $D_{1.06s}$ like those expected from conventional Stokes–Einstein theory (Supplementary Fig. 4c). In contrast, NPs in a stiff stress relaxing matrix exhibited a subdiffusive ($\alpha \approx 0.39$), slower ($D_{1.06s} \approx 0.01 \mu\text{m}^2 \text{s}^{-1}$) transport (Supplementary Fig. 4d), which indicates confinement. Strikingly, EVs in a stiff stress relaxing matrix showed α approaching that of NPs transporting in solution ($\alpha \approx 0.88$) (Fig. 3b,c). EVs in a soft stress relaxing matrix exhibited a significantly lower $D_{1.06s}$ (Fig. 3d) with subdiffusive transport ($\alpha \approx 0.49$), whereas EVs in a stiff elastic matrix showed a more pronounced subdiffusive transport ($\alpha \approx 0.045$), which indicates that the matrix stress relaxation allows EVs to overcome confinement.

Stress relaxing matrix systems can give rise to ‘dynamic heterogeneity’¹⁵ wherein particles can escape confinement or ‘cages’ formed by the matrix. To determine an expected s.d. of $D_{1.06s}$ for particles

in a homogeneous system, tracks were simulated matched to measurement conditions (Methods). Simulated tracks followed the measured tracks for NPs transporting in solutions (Supplementary Fig. 4e). The s.d. of experimentally determined $D_{1.06s}$ (σ_{meas}) was calculated and normalized to the s.d. of $D_{1.06s}$ for simulated trajectories (σ_{sim}) to measure the degree of heterogeneity of $D_{1.06s}$ (ref. ¹⁶). Although NPs in solution followed their simulated trajectories with a lower degree of heterogeneity, $\sigma_{\text{meas}}/\sigma_{\text{sim}}$ (Supplementary Fig. 4f), EVs in the matrix showed a higher $\sigma_{\text{meas}}/\sigma_{\text{sim}}$ (Fig. 3e), which indicates a more heterogeneous distribution of $D_{1.06s}$. To investigate this behaviour, we analysed how individual EVs exhibited changes in transport motions over time by defining another 3D diffusion coefficient ($D_{0.53s}$) with shorter intervals $\tau = 2\Delta t \approx 0.53$ s to capture the local transport behaviours. $D_{0.53s}$ was calculated for each interval τ_i within the tracks to express each track as $D_{0.53s}(\tau_i)$. Next, the difference of $D_{0.53s}(\tau_i)$ between consecutive intervals τ_i and τ_{i+1} ($\tau_1 \approx 0.53$ s, $\tau_2 \approx 1.06$ s, ...) was taken to calculate $\Delta D_{0.53s}$:

$$\Delta D_{0.53s}(\tau_i) = D_{0.53s}(\tau_{i+1}) - D_{0.53s}(\tau_i) \quad (4)$$

which indicates the magnitude of changes in the diffusion coefficient over time within a track. To compare the spread of $\Delta D_{0.53s}$ between groups, values for $\Delta D_{0.53s}$ were normalized to the mean $\Delta D_{0.53s}$ for each group (normalized $\Delta D_{0.53s}$). From a theoretical perspective, particle motion is facilitated when $\Delta D_{\tau} > 0$, particle motion is hindered when $\Delta D_{\tau} < 0$ and particle motion remains constant when $\Delta D_{\tau} \approx 0$ (Supplementary Fig. 5a). $\Delta D_{0.53s}$ values were close to zero for NPs transporting in solution (Supplementary Fig. 5b),

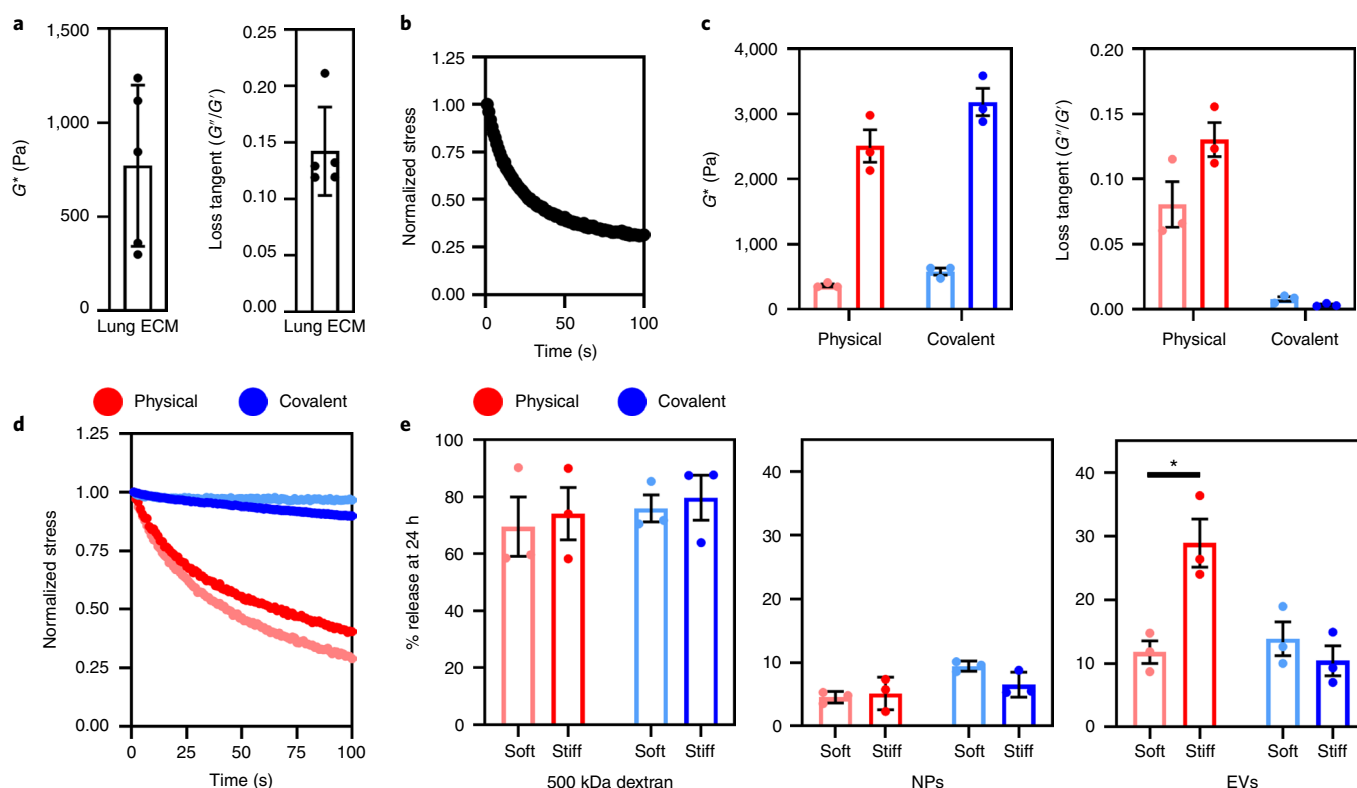


Fig. 2 | Complex shear modulus and stress relaxation time regulate the bulk release of EVs from hydrogels. **a**, Mean rheological properties of $N=5$ decellularized lung tissue slices calculated at 1 Hz: complex shear (left) modulus and loss tangent (right). **b**, Decellularized lung tissue exhibited stress relaxation with $t_{1/2}=14.9$ s. Data represent the mean of $N=3$ tissue slices. **c**, Rheological properties of the hydrogels calculated at 1 Hz: complex shear (left) modulus and loss tangent (right). **d**, Stress relaxation properties of the hydrogels. For **c** and **d**, the data represent the mean of $N=3$ hydrogels. Error bars are s.e.m. **e**, The release of EVs, but not of dextran or NPs, was affected by the hydrogel complex shear modulus for hydrogels that exhibit stress relaxation: 500 kDa dextran release from hydrogels (left), NP release from hydrogels (middle) and EV release from hydrogels (right). $N=3$ hydrogels across 3 independent experiments. Data represent the mean and error bars denote the s.e.m. * $P=0.0095$ via two-way analysis of variance (ANOVA) followed by Tukey's test for multiple comparisons. Unless stated otherwise, error bars denote s.e.m.

which suggests that $\Delta D_{0.53s} \approx 0$ for particles that undergo free diffusion. However, individual tracks of EVs in a stiff matrix showed a much broader distribution of $\Delta D_{0.53s}$ (Fig. 3f and Supplementary Fig. 5c,d), which suggests that a stiff matrix drives the fluctuating transport motions within the tracks. Furthermore, $\Delta D_{0.53s}$ values were $\sim 50\%$ both positive and negative (Supplementary Fig. 5e), which indicates that this behaviour is associated with zero-mean fluctuations in transport motion.

To calculate the extent to which EVs escaped confinement, we modelled the matrix as a system of 'cages' with a defined size c that transporting particles must overcome (Supplementary Fig. 6)^{17–19}. As NPs in a stiff stress relaxing matrix were confined with $\alpha \approx 0.39$, c was defined as the plateau MSD for this condition ($c \approx 0.09 \mu\text{m}^2$). Tracks were analysed to determine whether their MSD exceeded c (the fraction of particles that escapes from the cages) and, if so, the elapsed time before the MSD exceeded c (the escape time). A significant amount of the EVs in a stiff stress relaxing matrix demonstrated the ability to escape cages and they did this more rapidly (~ 1.3 s) than the EVs in a soft stress relaxing matrix (Fig. 3g). In contrast, EVs in a stiff elastic matrix less readily escaped cages, which further shows that matrix stress relaxation is crucial to allow EV transport. Furthermore, we calculated the radius of gyration R_g (ref. 20) for each particle, defined as the time-averaged root mean square displacement over the particle trajectory. EVs in a stiff stress relaxing matrix explored more space than EVs in a soft stress relaxing matrix, as indicated as by a higher R_g (Fig. 3h).

As the EVs showed the ability to transport in confined spaces, we hypothesized that intrinsic EV properties also drive their transport. Although lyophilized (freeze-dried) EVs possessed the same size distribution as freshly isolated EVs (Supplementary Fig. 7a), they did not exhibit a greater release from the stiff stress relaxing hydrogel (Fig. 4a)—this was further confirmed by a decrease in $D_{1.06s}$ by about tenfold and in α to ~ 0.25 . (Fig. 4b). Non-lyophilized EVs with an integral membrane structure are probably required for mechanically sensitive transport, as lyophilizing EVs²¹ can compromise their membrane integrity. This is supported by the addition of the cryoprotectant trehalose to EV preparations during lyophilization²², which recovers release behaviour (Supplementary Fig. 7b). We speculated that transport may be regulated by EV surface interactions within hydrogels or actomyosin contractility within EVs. However, tethering the integrin binding ligand RGD ($\sim 0.8 \mu\text{M}$) within hydrogels or treating hydrogels with drugs against myosin-II (blebbistatin) and Rho-associated protein kinase (Y27632) did not affect the EV release (Supplementary Fig. 7c,d). Importantly, ATP within EV preparations existed at a concentration much less than that in cells (Supplementary Fig. 7e), and EVs from cells partially ($\sim 50\%$) depleted of ATP do not release differently (Supplementary Fig. 7f), which indicates that EV transport mechanisms are probably metabolically passive rather than active.

Water permeation via aquaporins drives the migration of spatially confined cells independent of myosin-II²³. As aquaporins are partitioned into EVs²⁴, we hypothesized that water permeation

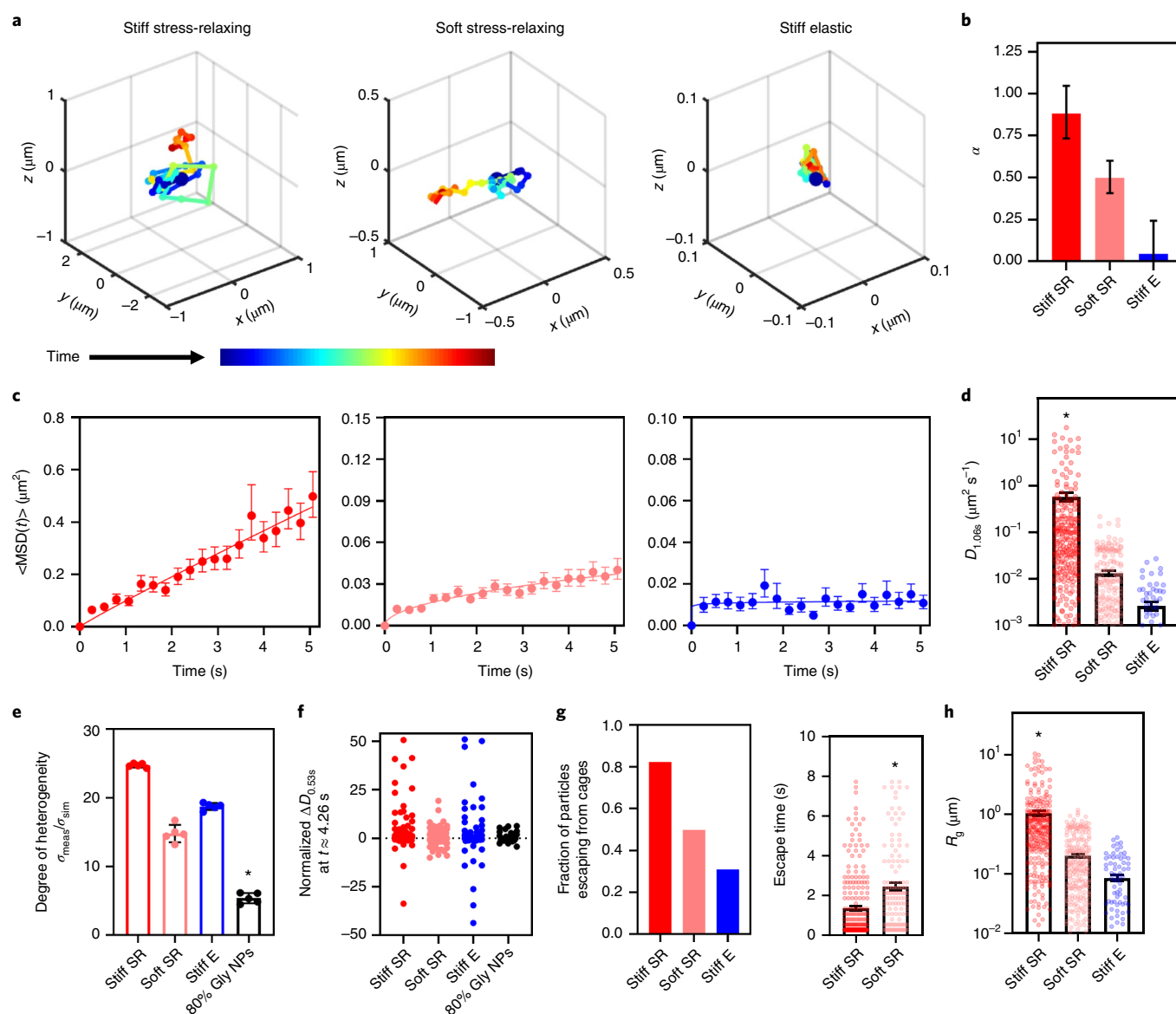


Fig. 3 | Individual EVs exhibit anomalous transport that is more rapid and diffusive in a stiff stress relaxing matrix. **a**, Representative 3D particle tracks for EVs in a matrix (Supplementary Videos). **b**, Values of α calculated for a non-linear fit of tracking data for EVs in the matrices (equation (1)). Error bars represent the 95% confidence interval. **c**, EVs in a stiff stress relaxing matrix (left, $N=279$) exhibit a more diffusive ensemble-averaged transport ($\alpha \approx 0.89$) relative to EVs in a soft stress relaxing (middle, $N=263$) or stiff elastic matrix (right, $N=89$). Data represent the mean and error bars represent s.e.m. **d**, Mean $D_{1,06s}$ calculated for the tracks in **b**. $*P=6.9 \times 10^{-7}$ via a one-way ANOVA with Tukey's test for multiple comparisons. **e**, EV transport in the matrix displays a dynamic heterogeneity, indicated by a higher s.d. of $D_{1,06s}$ for the measured tracks versus the simulated tracks, $\sigma_{\text{meas}}/\sigma_{\text{sim}}$. $N=5$ simulations. $*P < 10^{-15}$ via one-way ANOVA with Tukey's test for multiple comparisons. **f**, The distributions of the change in diffusion coefficient $\Delta D_{0.53s}$ calculated at $t \approx 4 \text{ s}$ are broader for EVs in a stiff matrix, which indicates a fluctuating motion. **g**, Escape from the cages of confinement for EV tracks in **b**: fraction of EVs able to escape cages (left) and time elapsed before the EVs escape the cages (right). $*P=7.5 \times 10^{-8}$ via an unpaired two-tailed t -test. **h**, R_g for EV tracks in **b**. $*P < 10^{-15}$ via one-way ANOVA with Tukey's test for multiple comparisons. Each tracking condition was performed across two independent experiments. For **e** and **f**, NPs in 80% glycerol were analysed for $N=32$ tracks. Unless stated otherwise, error bars denote s.e.m. SR, stress relaxing; E, elastic.

through aquaporins regulates EV transport. EV release in both stiff and soft stress relaxing hydrogels was increased by the addition of 3% polyethylene glycol (Fig. 4c), but did not occur if the EVs were freeze-dried (Supplementary Fig. 7g). We then tested whether aquaporins are required for EV release. AQP1 is the dominant aquaporin isoform expressed in MSCs (Supplementary Fig. 8a and Supplementary Table 1). Treating cells with short interfering RNA (siRNA) against AQP1 leads to an $\sim 80\%$ mRNA knockdown in cells (Supplementary Fig. 8b) and a $\sim 60\%$ reduction in the AQP1

protein packaged into EVs (Supplementary Fig. 8c). AQP1 depletion in EVs significantly increased their Young's modulus (Fig. 4d and Supplementary Figs. 9a,b), which suggests that water permeation makes the EVs more deformable. AQP1 depletion in EVs significantly decreased the EV release from hydrogels (Fig. 4e), and AQP1-depleted EVs showed an impaired release from decellularized matrices (Fig. 4f and Supplementary Fig. 9c), which indicates that the greater deformability via AQP1 enhances the EVs ability to transport in the matrix. Although AQP1 depletion

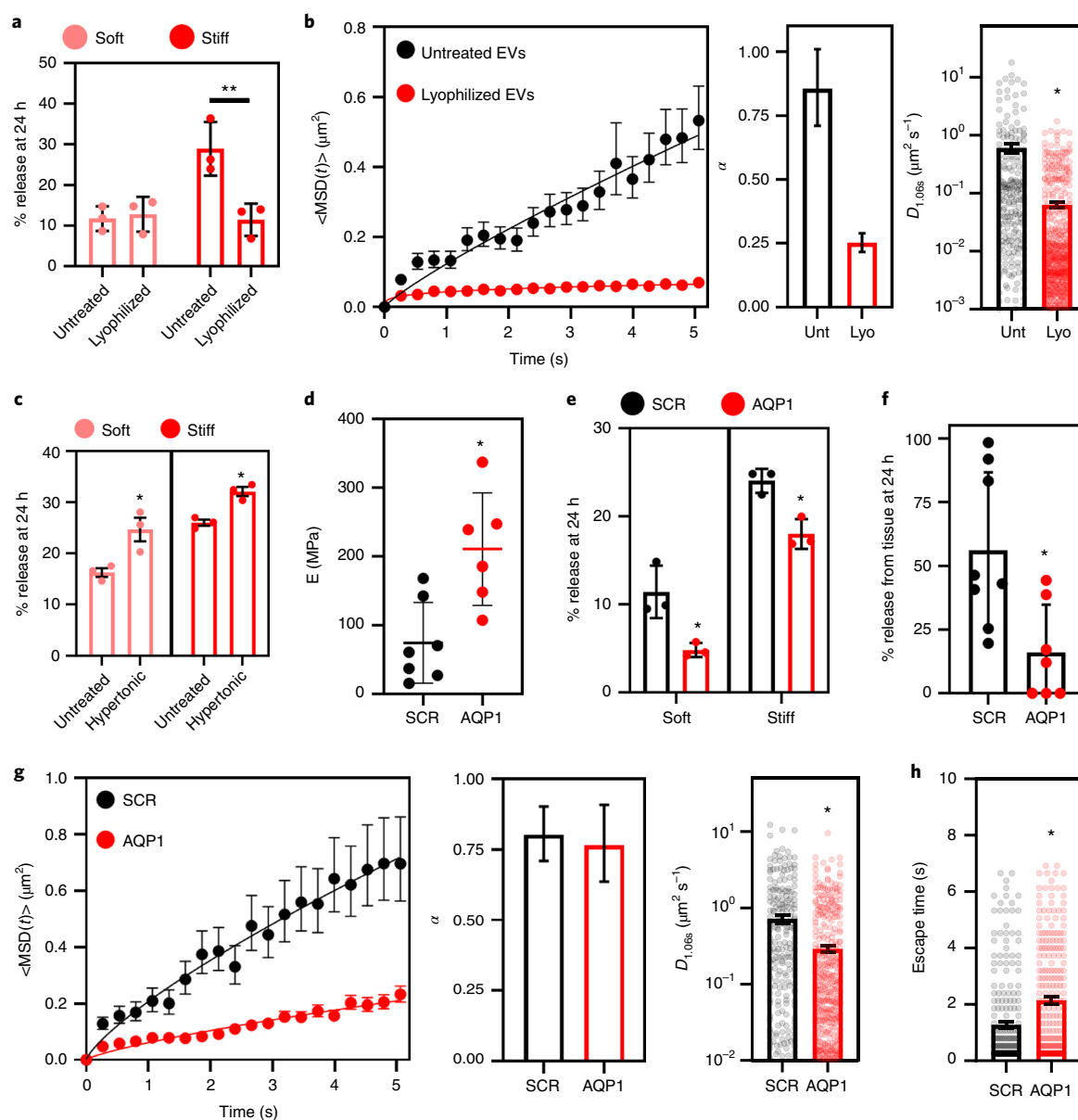


Fig. 4 | Aquaporin-1 mediates the ability of EVs to transport in engineered and decellularized matrices by increasing the EV deformability. **a**, After lyophilization, the mean % EV release decreased from stiff stress relaxing hydrogels. $N=3$ hydrogels for each condition. $^{**}P=0.012$ via two-way ANOVA followed by Tukey's test for multiple comparisons. **b**, Ensemble MSD curves for untreated (Unt; $N=279$) versus lyophilized (Lyo; $N=618$) EV tracks in a stiff stress relaxing matrix (left). Values of α from a non-linear fit by equation (1) (middle). Error bars represent the 95% confidence interval. Mean $D_{1.06s}$ (right). $^{*}P=2.9 \times 10^{-12}$ via an unpaired two-tailed t -test. **c**, Hypertonic medium (3% polyethylene glycol, 300 kDa) significantly increased the mean % EV released from stress relaxing hydrogels. $N=3$ hydrogels for each condition. $^{*}P=0.026$ (soft), $P=5 \times 10^{-3}$ (stiff) via an unpaired two-tailed t -test. **d**, EVs from cells treated with siRNA against AQP1 ($N=6$) exhibited a significantly higher mean Young's modulus (E) than EVs from cells treated with a scrambled siRNA control (SCR, $N=7$). $^{*}P=0.005$ via an unpaired two-tailed t -test. **e**, EVs depleted of AQP1 exhibited a significantly lower mean % released from stress relaxing hydrogels. $N=3$ hydrogels for each condition. $^{*}P=0.021$ (soft), $P=8.6 \times 10^{-3}$ (stiff) via an unpaired two-tailed t -test. **f**, The mean % release of AQP1-depleted EVs ($N=7$) from decellularized lung tissue was significantly reduced versus a control ($N=8$). $^{*}P=0.010$ via an unpaired two-tailed t -test. **g**, Ensemble MSD curves (left) for AQP1-depleted EV tracks ($N=613$) versus control ($N=659$) EV tracks. AQP1-depletion did not change the α values (middle). Error bars are the 95% confidence interval. AQP1-depletion significantly decreased the mean $D_{1.06s}$ (right). $^{*}P=1.3 \times 10^{-8}$ via an unpaired two-tailed t -test. **h**, From an analysis of the tracks from **g**, AQP1-depleted EVs exhibited a significantly slower mean escape time than that of the control EVs in a stiff stress relaxing matrix. $^{*}P=2.1 \times 10^{-7}$ via an unpaired two-tailed t -test. Unless stated otherwise, the error bars denote s.e.m.

reduced $D_{1.06s}$ by about threefold, α remained unchanged for individual EVs (Fig. 4g). Liposomes encapsulated in the stiff stress relaxing matrix exhibited $\alpha \approx 0.65$ (Supplementary Fig. 9d) with a much lower $D_{1.06s}$ (Supplementary Fig. 9e), which suggests that the presence of lipid membrane alone is not sufficient

for an enhanced EV transport. Pulling values from all the experimental groups of EVs in a matrix shows that α increases with increased $D_{1.06s}$, but becomes saturated near $\alpha \approx 1.0$ when $D_{1.06s}$ is higher than $0.1 \mu\text{m}^2 \text{s}^{-1}$ (Supplementary Fig. 9f), which suggests that a threefold decrease in $D_{1.06s}$ via AQP1 depletion is

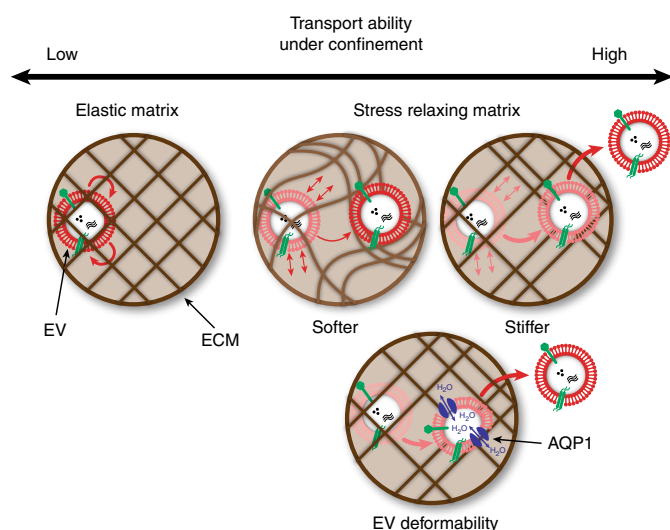


Fig. 5 | Model for EV transport under confinement. EVs exist trapped in an elastic matrix, whereas matrix stress relaxation allows EVs to escape confinement. Stiffness in a stress relaxing matrix leads to fluctuating transport motions, which further increases EVs ability to transport. Furthermore, AQP1 present on EVs mediates water permeation within the EVs, which leads to a greater EV deformability and enhanced transport under confinement.

less likely to be sufficient to significantly decrease α . Consistent with these results, AQP1 depletion decreased the time required for EVs to escape cages (Fig. 4h). Finally, AQP1 depletion did not affect the spread of $\Delta D_{0.53s}$ (Supplementary Fig. 9g), which indicates the independence of AQP1 with fluctuating transport motion.

The results describe the ability of EVs to transport in a polymer matrix with an absence of matrix degradation, despite EVs being larger than the average mesh size of the matrices. The matrix stress relaxation allowed the EVs to readily escape cages formed by the polymer network (Fig. 5). A stiff matrix increased the fluctuating EV transport motions, and thus the combination of stiffness and stress relaxation led to a greatly enhanced EV transport. EVs were also subjected to water permeation through AQP1, which allowed the EVs to become more deformable by altering their volume, which enabled their escape from confinement. This behaviour is reminiscent of a model of the hopping diffusion of nanoparticles in entangled polymer matrices^{25–27}, in which it is hypothesized that nanoparticles show the ability to slide through a matrix under some conditions. The phospholipid content of EVs vary²⁸, and thus it will be interesting to determine whether and how these contents affect EV transport in matrix, as lipid asymmetry was shown to affect EV membrane stability²⁹. The observation that AQP1 mediates EV deformability and the resulting transport in ECM is important because the deformability of synthetic nanoparticles with lipid bilayers was recently shown to dramatically affect their accumulation in tissues both in vitro and in vivo³⁰. Future studies will test whether the presence of water channels on lipid vesicles alone is sufficient or if other membrane components are also necessary to facilitate EV transport under confinement in matrix. Furthermore, the 3D particle tracking approach utilized here can be extended to study EV transport in various environments, for investigating or treating diseases implicating EVs. Finally, the results may inform how therapeutic EVs can potentially be modified to better facilitate their delivery through tissue ECM. In summary, this study opens new avenues of investigations into EV transport behaviours that occur in the ECM.

Online content

Any methods, additional references, Nature Research reporting summaries, source data, extended data, supplementary information, acknowledgements, peer review information; details of author contributions and competing interests; and statements of data and code availability are available at <https://doi.org/10.1038/s41565-020-0636-2>.

Received: 19 August 2019; Accepted: 9 January 2020;

Published online: 17 February 2020

References

- Huleihel, L. et al. Matrix-bound nanovesicles within ECM bioscaffold. *Sci. Adv.* **6**, e1600502 (2015).
- Meldolesi, J. Exosomes and ectosomes in intercellular communication. *Curr. Biol.* **28**, R435–R444 (2018).
- Tomlins, P., Grant, P., Mikhalovsky, S., James, S. & Mikhalovska, L. Measurement of pore size and porosity of tissue scaffolds. *J. ASTM Int.* **1**, 1–8 (2004).
- Luker, K. E. et al. Comparative study reveals better far-red fluorescent protein for whole body imaging. *Sci. Rep.* **5**, 10332 (2015).
- Rakian, R. et al. Native extracellular matrix preserves mesenchymal stem cell ‘stemness’ and differentiation potential under serum-free culture conditions. *Stem Cell Res. Ther.* **6**, 235 (2015).
- Vining, K. H., Stafford, A. & Mooney, D. J. Sequential modes of crosslinking tune viscoelasticity of cell-instructive hydrogels. *Biomaterials* **188**, 187–197 (2019).
- Lee, K. Y. & Mooney, D. J. Alginate: properties and biomedical applications. *Prog. Polym. Sci.* **37**, 106–126 (2012).
- Chaudhuri, O. et al. Hydrogels with tunable stress relaxation regulate stem cell fate and activity. *Nat. Mater.* **15**, 326–334 (2016).
- Grant, G. T., Morris, E. R., Rees, D. A., Smith, P. J. C. & Thom, D. Biological interactions between polysaccharides and divalent cations: the egg-box model. *FEBS Lett.* **32**, 195–198 (1973).
- Armstrong, J. K., Wenby, R. B., Meiselman, H. J. & Fisher, T. C. The hydrodynamic radii of macromolecules and their effect on red blood cell aggregation. *Biophys. J.* **87**, 4259–4270 (2004).
- Skotland, T., Hessvik, N. P., Sandvig, K. & Llorente, A. Exosomal lipid composition and the role of ether lipids and phosphoinositides in exosome biology. *J. Lipid Res.* **60**, 9–18 (2019).
- Branco da Cunha, C. et al. Influence of the stiffness of three-dimensional alginate/collagen-I interpenetrating networks on fibroblast biology. *Biomaterials* **35**, 8927–8936 (2014).
- Metzler, R., Jeon, J. H., Cherstvy, A. G. & Barkai, E. Anomalous diffusion models and their properties: non-stationarity, non-ergodicity, and ageing at the centenary of single particle tracking. *Phys. Chem. Chem. Phys.* **16**, 24128–24164 (2014).
- Etoc, F. et al. Non-specific interactions govern cytosolic diffusion of nanosized objects in mammalian cells. *Nat. Mater.* **17**, 740–746 (2018).
- Schirmache, W., Ruocco, G. & Mazzone, V. Heterogeneous viscoelasticity: a combined theory of dynamic and elastic heterogeneity. *Phys. Rev. Lett.* **115**, 015901 (2015).
- Lieleg, O., Vladescu, I. & Ribbeck, K. Characterization of particle translocation through mucin hydrogels. *Biophys. J.* **98**, 1782–1789 (2010).
- Goiko, M., De Bruyn, J. R. & Heit, B. Short-lived cages restrict protein diffusion in the plasma membrane. *Sci. Rep.* **6**, 34987 (2016).
- Weigel, A. V., Simon, B., Tamkun, M. M. & Krapf, D. Ergodic and nonergodic processes coexist in the plasma membrane as observed by single-molecule tracking. *Proc. Natl Acad. Sci. USA* **108**, 6438–6443 (2011).
- Manzo, C. et al. Weak ergodicity breaking of receptor motion in living cells stemming from random diffusivity. *Phys. Rev. X* **5**, 011021 (2015).
- Parry, B. R. et al. The bacterial cytoplasm has glass-like properties and is fluidized by metabolic activity. *Cell* **156**, 183–194 (2014).
- Kusuma, G. D. et al. To protect and to preserve: novel preservation strategies for extracellular vesicles. *Front. Pharmacol.* **9**, 01199 (2018).
- Frank, J. et al. Extracellular vesicles protect glucuronidase model enzymes during freeze-drying. *Sci. Rep.* **8**, 12377 (2018).
- Stroka, K. M. et al. Water permeation drives tumor cell migration in confined microenvironments. *Cell* **157**, 611–623 (2014).
- Blanc, L. et al. The water channel aquaporin-1 partitions into exosomes during reticulocyte maturation: implication for the regulation of cell volume. *Blood* **114**, 3928–3934 (2009).
- Cai, L. H., Panyukov, S. & Rubinstein, M. Hopping diffusion of nanoparticles in polymer matrices. *Macromolecules* **48**, 847–862 (2015).
- Wong, I. Y. et al. Anomalous diffusion probes microstructure dynamics of entangled F-actin networks. *Phys. Rev. Lett.* **92**, 178101 (2004).
- Ritchie, K. et al. Detection of non-Brownian diffusion in the cell membrane in single molecule tracking. *Biophys. J.* **88**, 2266–2277 (2005).

28. Mathieu, M., Martin-Jaular, L., Lavieu, G. & Théry, C. Specificities of secretion and uptake of exosomes and other extracellular vesicles for cell-to-cell communication. *Nat. Cell Biol.* **21**, 9–17 (2019).
29. Manno, S., Takakuwa, Y. & Mohandas, N. Identification of a functional role for lipid asymmetry in biological membranes: phosphatidylserine-skeletal protein interactions modulate membrane stability. *Proc. Natl Acad. Sci. USA* **99**, 1943–1948 (2002).

30. Guo, P. et al. Nanoparticle elasticity directs tumor uptake. *Nat. Commun.* **9**, 130 (2018).

Publisher's note Springer Nature remains neutral with regard to jurisdictional claims in published maps and institutional affiliations.

© The Author(s), under exclusive licence to Springer Nature Limited 2020

Methods

Particle size and number characterization. Particle size and number were obtained using a Nanoparticle Tracking Analysis 3.2 via a NanoSight NS300 (Malvern) with a 405 nm laser. Samples were introduced by a syringe pump at a rate 100 $\mu\text{l min}^{-1}$. Three 30 s videos were acquired using camera level 14 followed by detection threshold 7. Camera focus, shutter, blur, minimum track length, minimum expected particle size and maximum jump length were set automatically by the software. Samples were diluted as needed to maintain particles per video from 100 to 2,000.

Cell culture. All cells were cultured at 37°C in 5% CO₂. HeLa cells (CCL-2, ATCC) were a gift from A. Karginov at the University of Illinois at Chicago (UIC). D1 MSC cells (CRL-12424, ATCC), HeLa cells and HEK293T cells (CRL-3216, ATCC) were cultured using high-glucose DMEM (Thermo) supplemented with 10% FBS (Atlanta Biologicals), 1% penicillin/streptomycin (P/S; Thermo) and 1% GlutaMAX (Thermo) to 80% confluency before passaging, no more than 30 times. Human umbilical vein endothelial cells (HUVEC) (no. CC-2519, Lonza) were a gift from Y. Komarova at UIC. HUVEC were cultured using Ham's F-12K (Thermo) supplemented with 10% FBS, 1% P/S, 1% GlutaMAX, 0.1 mg ml⁻¹ heparin (no. H3393, Sigma) and endothelial cell growth supplement (no. E2759, Sigma) at passage 5. Human MSCs (hMSCs) were derived by the plastic adherence of mononucleated cells from human bone marrow aspirate (Lonza). After 3 days, the adherent cells were cultured in the hMSC medium: α -minimal essential medium (Thermo) supplemented with 20% FBS, 1% P/S (Thermo Fisher Scientific) and 1% GlutaMAX (Thermo). After reaching 70–80% confluence at 10–14 days, the cells were split, expanded in the hMSC medium and used at passage 3. Cells were routinely tested for mycoplasma contamination and only used if no contamination was present.

Lentiviral expression of CD63 fused with K2S. A DNA plasmid that contained K2S was synthesized in a pUC57-Kan backbone (GenScript). The K2S sequence was cloned into a lentiviral construct that contained CD63 (LV112335, Applied Biological Materials) so that K2S fused to CD63 on the C terminus of CD63. D1 MSCs were transduced with lentivirus that contained the CD63–K2S plasmid using standard techniques³¹. Briefly, lentiviral particles were produced with a second-generation lentiviral packaging system (LV003, Applied Biological Materials) using Lentifectin (Applied Biological Materials) in HEK293T cells. Lentiviral particles were purified and applied to D1 MSCs at passage 10 with 8 $\mu\text{g ml}^{-1}$ polybrene (Sigma) for 3 days. Cells were expanded over a period of several days to reach ~80% confluency. Then, cells were sorted using a MoFlo Astrios (Beckman Coulter) based on their CD63–K2S signal compared to those of non-transduced cells of the same passage. Concentrated EV solutions were shown to be positive for CD63–K2S versus EVs from non-transduced cells using IVIS imaging (Living Image 4.0, Perkin Elmer).

Extracellular vesicle isolation and preparation. To isolate EVs from cells, the cells were washed twice with Hank's balanced salt solution (HBSS; Thermo) followed by incubation with serum-free growth medium for 1 h. Afterwards, the medium was exchanged with a medium that consisted of high-glucose DMEM supplemented with 10% exosome-depleted FBS (Thermo) instead of 10% FBS. The next day, the medium was centrifuged at 2,000g for 10 min to remove cell debris followed by centrifugation at 10,000g to remove particles larger than 500 nm (ref. ³²). Afterwards, the solution was added to a 100 kDa MW-cutoff column (Amicon) and centrifuged at 5,000g for 20 min followed by washing with an equal volume of HBSS. The retentate was resuspended and confirmed to contain concentrated EVs using NanoSight NS300 (Malvern).

Lyophilization of EVs. Concentrated EVs were frozen at –80°C overnight. If applicable, the preparations were treated with 4% trehalose (Sigma) before freezing. They were then placed in a lyophilization chamber operating at <0.1 mbar vacuum and <–100°C temperature and allowed to sublimate overnight. The solid was reconstituted in HBSS and confirmed to contain EVs using NanoSight NS300.

Decellularization of lung tissues. All animal procedures were performed in compliance with National Institutes of Health and institutional guidelines approved by the ethical committee from UIC. Female C57BL/6J mice were purchased from The Jackson Laboratory, housed in the UIC Biologic Resources Laboratory and killed 12 weeks after birth. Lung tissue was harvested and decellularized based on techniques described previously³³. Briefly, the heart–lung bloc was exposed and the trachea cannulated with a blunted 18-gauge needle. Lungs were infused with 1 ml of deionized water that contained 5% P/S (wash solution). The heart–lung bloc was excised and washed through the airway and the right ventricle, incubated in a 0.1% Triton-X wash solution overnight at 4°C, washed and incubated in a 2% sodium deoxycholate wash solution overnight at 4°C. It was then washed, incubated in a 1 M NaCl wash solution for 1 h at room temperature, washed and incubated in a wash solution that contained DNAase for 1 h at room temperature. The tissue was placed in a solution of liquified 5% low-melting-point agarose (GeneMate) and allowed to solidify at 4°C overnight. Slices were prepared using a tissue slicer (Brintree) into 1 mm sections and punched into 5 mm discs using a punch (Integra). Discs were placed in HBSS, incubated at 42°C for 30 min and washed several times.

Multiphoton microscopy. About 1 \times 10⁹ CD63–K2S EVs were incubated with a ~5 mm tissue slice at 37°C for 3 days followed by washout. EV-loaded tissue slices were imaged using a \times 20 1.00 NA water immersion objective (Olympus) with a multiphoton microscope (Bruker Fluorescence Microscopy) equipped with a Coherent Cameleon Ultra II laser that employed both second harmonic and two-photon excited fluorescence signal generation³⁴. Backward-scattering second harmonic generation was obtained at 860 nm excitation to capture signals from collagen within tissue and two-photon excited fluorescence generation was performed at 760 nm excitation to capture signals from CD63–K2S. Three images were taken each for experimental and background (no loaded EVs) conditions. Images were processed by subtracting background fluorescence from the 760 nm channel. Then, three regions of interest were chosen for each background-subtracted image and Pearson's correlation coefficient was calculated. Next, the 760 nm channel signal was randomized using the MATLAB function RANDBLOCK³⁵. Pearson's correlation coefficient calculated again and the distributions compared.

Lung-tissue transport experiments. After loading ~1 \times 10⁹ CD63–K2S EVs onto a ~5 mm tissue slice for 3 days, the loading was confirmed using IVIS. The EV transport was determined by measuring tissue fluorescence before and after the indicated times. Imaging occurred with a 3 s exposure using a fluorescence excitation filter at 570 nm and an emission filter at 640 nm. IVIS software (Living Image 4.0, Perkin Elmer) was used to create a region of interest around the tissue pieces where the total fluorescent signal was counted.

Material preparation and hydrogel formation. Raw sodium alginates with different molecular weights, low (5/60, ~40 kDa) and medium (10/60, ~120 kDa), were obtained from FMC Corporation. Alginate was purified through dialysis in a 3.5 kDa membrane submerged in water, followed by treatment with activated charcoal (Sigma) 0.5 g per gram alginate. It was then filtered, frozen and lyophilized to obtain a solid polymer. Conjugation of click chemistry reagents or RGD (amino acid sequence GGGGRGDSP, Peptide 2.0) to alginate polymers was performed using a method described previously³⁶. 1-bicyclo[2.2.1]hept-5-en-ylmethanamine (norbornene amine, Matrix Scientific) was conjugated to 10/60 alginate at degree of substitution (DS) 75–150 and tetrazine-amine (Conju-Probe) was conjugated to 5/60 alginate to achieve a DS18–36. For some experiments, RGD was conjugated to 10/60 alginate at DS10. Physically crosslinked hydrogels were formed as described previously³⁷. Briefly, alginate solutions were mixed to be 1% 5/60 and 1% 10/60 (2% total), added to a syringe and locked to another syringe with CaSO₄ (Sigma) to achieve final calcium concentrations of 12 mM (soft) and 20 mM (stiff). After mixing, the solutions were deposited under glass for 2 h to form a hydrogel. For covalently crosslinked hydrogels, tetrazine-alginate and norbornene-alginate were mixed to be 1% each (2% total), and deposited under glass for 2 h to form a hydrogel. Interpenetrating network hydrogels of collagen-1 and alginate were created as described¹². Briefly, hydrogels were prepared as physically crosslinked hydrogels, but the solution was mixed with collagen-I to achieve a final concentration of 0.75 or 0.375 mg mL⁻¹ before mixing with CaSO₄. To avoid drying, hydrogels were incubated in a 'retention medium': HEPES-buffered saline at pH 7.75 supplemented with 2 mM CaCl₂, an amount shown previously⁷ to prevent the leaching of calcium from hydrogels without leading to further crosslinking.

Mechanical characterization of hydrogels and tissues. The mechanical properties of hydrogels or tissues were obtained using rheometry via Anton Paar MCR302. Storage (G') and loss (G'') moduli were measured through a frequency sweep by lowering the geometry (Anton Paar PP08) to a 5% normal strain followed by a rotation that induced a 0.5% shear strain at an increasing frequency and finally measurement of the resulting shear stress. The complex shear modulus G^* was calculated³⁸:

$$G^* = \sqrt{G'^2 + G''^2} \quad (5)$$

The loss tangent was defined as:

$$\tan\delta = G''/G' \quad (6)$$

To determine the stress relaxation, the geometry was lowered at constant velocity (25 $\mu\text{m s}^{-1}$) through the linear elastic region until a 15% strain was reached. Swelling ratios were calculated by leaving samples to dry or swell overnight followed by mass measurements. The swelling ratio Q was calculated through the volumes of hydrogels expressed as^{39,40}:

$$V_s = \frac{m_d}{m_s} = \frac{1}{Q}; V_r = \frac{m_d}{m_r} \quad (7)$$

where m is the hydrogel weight and subscripts d, r and s denote dry, relaxed (before swelling) and swollen hydrogels. The average molecular weight between the crosslinks was calculated as:

$$1/\bar{M}_C = 2/\bar{M}_n - \frac{(\bar{v}/V) [\ln(1 - V_s) + V_s + \chi V_s^2]}{V_r [(V_s/V_r)^{1/3} - V_s/2V_r]} \quad (8)$$

with \bar{M}_n is the average molecular weight of polymers, \bar{V}/V the molar volume of hydrogel divided by the molar volume of water and χ the Flory interaction parameter. The values were used to calculate the average hydrogel mesh size ξ through equation (9):

$$\xi = V_s^{-1/3} \left(\frac{2CM_c}{\bar{M}_r} \right)^{1/2} l \quad (9)$$

with C the polymer characteristic ratio, \bar{M}_r the average molecular weight of the polymer repeating unit and l the carbon–carbon bond length. Differential scanning calorimetry was used to perform thermoporometry to measure the pore size distributions as described previously⁴¹. Briefly, samples ~10 mg were placed in a sealable aluminium pan inside the differential scanning calorimetry instrument (TA Instruments Q2000). Samples were cooled to -30°C at a rate of 4°C min^{-1} , held for 5 min, warmed to 15°C at a rate of 4°C min^{-1} , held for 5 min and then cooled again to -30°C at 4°C min^{-1} . Distributions were calculated by determining $\Delta V/\Delta R_p$ (ref. 42), where R_p is the pore radius, and then fitted to a frequency-normalized histogram.

Bulk transport experiments. Liposomes (FormuMax, no, F60103F-F) were obtained with a similar (~45% cholesterol, ~55% phospholipids) content as that of the EVs¹¹. The encapsulation of particles or dextran in bulk alginate hydrogels was performed by mixing particles with alginate or click alginate followed by hydrogel formation. The hydrogels were punched into discs and placed into polystyrene plates with retention medium. If applicable, the hydrogels were treated with blebbistatin (Cayman 13013) or Y-27632 (Cayman 10005583). If necessary, gels were digested by adding medium with 3.4 mg ml^{-1} alginate lyase (Sigma) and placing at 37°C for 30 min. Release was measured using fluorescence for polystyrene nanoparticles (SpheroTech) and FITC-dextran (500 kDa, Sigma). Percent release was determined at the indicated times as the number of particles in the medium P_M divided by P_M plus the number of particles in the digested hydrogel P_G as:

$$\% \text{ release} = \frac{P_M}{P_M + P_G} \times 100\% \quad (10)$$

For EVs and liposomes, P_M was measured as above using NanoSight NS300, but P_G was determined by calculating the initial number of particles added to the hydrogel using NanoSight NS300. Samples without encapsulated particles were used to account for background.

3D single-particle tracking. CD63-K2S EVs were encapsulated in hydrogels, placed on dishes of no. 1.5 coverslip thickness (MatTek), and imaged at $\times 60$ with immersion oil of refractive index 1.518 (Cargille) using a DeltaVision OMX microscope (GE). Single channel $1,024 \times 1,024$ pixel ($81.92 \times 81.92 \mu\text{m}$) images were obtained in $2 \mu\text{m}$ thick stacks with $0.125 \mu\text{m}$ spacing (16 images per stack) using the conventional imaging mode. Over ~8 s, 30 stacks were acquired for a stack frequency of 3.75 Hz and image frequency of 60 Hz. After acquisition, the images were processed through deconvolution using softWoRx.

Using the IMARIS 'Spots' function, a custom particle tracking algorithm was created. Particles were determined using intensity thresholding over regions that measured $10 \times 10 \times 1$ pixels followed by tracking their 3D position (x, y, z) over time (t). Tracks could continue if the particle was undetectable for a single timepoint within the track but not for two or more consecutive timepoints.

Analysis of particle-tracking data. Mathematical calculations and analysis were performed using MATLAB software. The particle MSD was calculated from the positional data as:

$$\text{MSD}(t) = [x(t) - x(t=0)]^2 + [y(t) - y(t=0)]^2 + [z(t) - z(t=0)]^2 \quad (11)$$

Tracks with less than five measurements of MSD were removed from further analysis. For ensemble-averaged tracks, a lower limit of 20 points and an upper limit of 30 points were defined to constrain the tracks considered for analysis, as uneven track sizes can bias the results¹⁴. Owing to this, the data are shown only up to the lower limit of 20 points ($t \approx 5$ s). To account for static (or localization) error⁴³, for each particle type, particles were adhered to glass using (3-aminopropyl) trimethoxysilane (Sigma) with a method described previously⁴⁴. The MSD was tracked for adherent particles over time, and the static error was defined as the plateau MSD. This error was subtracted from all subsequent MSD measurements for each experimental group.

Ensemble-averaged track data were generated by averaging the MSD for each track i at every time t elapsed since the start of tracking:

$$\langle \text{MSD}(t) \rangle = \frac{1}{N} \sum_{i=1}^N \text{MSD}_i(t) \quad (12)$$

where N is number of tracks. Exponent α was calculated for ensemble-averaged tracks using equation (1). Diffusion coefficient $D_{1.06\text{s}}$ was calculated over intervals $\tau = 4\Delta t \approx 1.06$ s for each track, as in equation (3). Thus, if the total track time is T , a given track has T/τ values for $D_{1.06\text{s}}(\tau)$, which were averaged to provide a singular

value for $D_{1.06\text{s}}$ for a given track. The expected $D_{1.06\text{s}}$ for particles was determined based on the Stokes–Einstein relationship:

$$D = \frac{k_B T}{6\pi\eta r} \quad (13)$$

where $k_B T$ is the Boltzmann constant multiplied by temperature, r is the particle radius and η is the solution viscosity. The viscosity of glycerol solutions was determined previously⁴⁵. The degree of heterogeneity of $D_{1.06\text{s}}$ was defined as described in the main text. For each sample, simulations were performed to obtain an equal number of simulated tracks as the number of tracks measured for each sample. Each $\text{MSD}(t)$ was drawn randomly from a zero-mean Gaussian distribution determined for each sample with variance $2D_{1.06\text{s}} t^{1/4}$. $D_{1.06\text{s}}$ was then calculated for simulated tracks as for experimental measurements (Eq. 2). 'Cages' of confinement were defined in the text. Tracks were evaluated for their ability to overcome this cage size by exceeding c (particles escaping) or not (particles not escaping). The timepoint at which the particle exceeds c is defined as the escape time. R_g was defined as the time-averaged root mean square displacement of particle tracks as:

$$R_g = \left[\frac{1}{N} \sum_{i=0}^N \text{MSD}(t_i) \right]^{1/2} \quad (14)$$

over each measured timepoint t_i through the duration of the track.

ATP measurement and pharmacological depletion. ATP concentration was measured using a commercially available luciferase-based assay (Cayman, 700410). Briefly, samples were lysed followed by the addition of a mixture that catalyses a reaction to produce bioluminescence based on the concentration of ATP within the samples. Values of bioluminescence were compared to a standard curve with a known concentration of ATP. To deplete ATP, the cells were treated with $1 \mu\text{g ml}^{-1}$ oligomycin (Cayman, 1404-19-9) and 1 mM 2-deoxy-D-glucose (Cayman, 154-17-6) for 24 h.

siRNA transfection. Scrambled siRNA (Dharmacon) or siRNA against AQP1 (AM16708, Ambion) was diluted to 160 nM in unsupplemented Opti-MEM medium (Thermo) and combined 1:1 with Opti-MEM supplemented with 2% Lipofectamine RNAiMAX (Thermo) and incubated at room temperature for at least 20 min. Cells were washed with HBSS and fresh growth medium was added to cells. The transfection solution was added dropwise for a final siRNA concentration of 4 nM and cells were incubated for 3 days followed by EV isolation.

Gene expression analysis. Trizol (Thermo Fisher Scientific) was added directly to cells. Chloroform ($200 \mu\text{l}$) was added per 1 ml of Trizol followed by centrifugation for 15 min at $15,000 \text{ r.p.m.}$ and 4°C . The top layer was collected and RNA precipitated with $500 \mu\text{l}$ of isopropanol for 20 min at 4°C . Samples were centrifuged at $12,500 \text{ r.p.m.}$ for 15 min at 4°C . The supernatant was removed, precipitated RNA was washed with 75% EtOH and centrifuged for 5 min at $7,500 \text{ r.p.m.}$ and 4°C . EtOH was removed and the purified RNA was resuspended in $15 \mu\text{l}$ of RNase-free water. The RNA concentration was quantified by NanoDrop. Complementary DNA was reverse transcribed by SuperScript-III (Thermo Fisher Scientific). qPCR was performed in the ViiA7 qPCR system with PowerSYBR Green master mix (Applied Biosystem). Samples were analysed in triplicate with 50 ng of complementary DNA per well. Relative gene expression was computed by the delta–delta threshold cycle method by comparing threshold cycle values to those of a reference gene (*GAPDH*). Supplementary Table 1 shows the list of primers for qPCR.

Atomic force microscopy. Vesicles were adhered to freshly cleaved mica by incubation at room temperature for 15 min followed by washing⁴⁴. Atomic force microscopy was performed using an MFP-3D-Bio model (Asylum Research) with a pyramidal tip (Bruker; MLCT, triangular, resonant frequency ~125 kHz) as described previously³⁰. Briefly, vesicles with a size range between about 50 and 300 nm were found by scanning in a tapping (a.c.) mode and indented until they reached 0.5 nN at 250 nm s^{-1} to generate a force–displacement curve. The data were analysed and converted to Young's modulus (E) using MATLAB by modelling the EVs as thin elastic shells⁴⁶. The slope of the approach curve was calculated over a sliding interval and the surface of the vesicle was determined by a high and sustained change in the slope. The linear region was used to calculate E via the equation

$$F(\delta) = \frac{aEt^2}{r} \delta \quad (15)$$

with F as the measured cantilever force and δ as the tip displacement. The constant a^2/r is determined by the vesicle geometry and assumed to be $\sim 0.87 \text{ nm}$.

Western blot. Western blot was performed using conventional methods on samples prepared by RIPA buffer. For each lane, $20 \mu\text{g}$ of protein was added. Immunoblots were performed against AQP1 (sc-20810, SCBT, 1:2000) and GAPDH (600004-1-Ig, Proteintech, 1:5000) using an anti-rabbit or anti-mouse HRP-conjugate secondary antibody (rabbit: 115-035-003; mouse: 115-035-071, Jackson ImmunoResearch Laboratories) combined with Luminol (Santa Cruz) substrate for detection.

Statistical evaluation. Statistics were performed as described in the figure captions. All statistical analyses were performed using GraphPad Prism version 8.1.1. Unless otherwise noted, the statistical comparisons were made from at least three independent experiments by one-way ANOVA followed by Tukey's multiple comparison test, and then were considered significant if $P < 0.05$.

Reporting summary. Further information on research design is available in the Nature Research Reporting Summary linked to this article.

Data availability

The data that support the plots within this paper and other findings of this study are available from the corresponding author upon reasonable request.

Code availability

The codes used to analyse the data in this study are available from the corresponding author upon reasonable request.

References

31. McGinley, L. et al. Lentiviral vector mediated modification of mesenchymal stem cells & enhanced survival in an in vitro model of ischaemia. *Stem Cell Res. Ther.* **2**, 12 (2011).
32. Lobb, R. J. et al. Optimized exosome isolation protocol for cell culture supernatant and human plasma. *J. Extracell. Vesicles* **4**, 27031 (2015).
33. Bonenfant, N. R. et al. The effects of storage and sterilization on de-cellularized and re-cellularized whole lung. *Biomaterials* **34**, 3231–3245 (2013).
34. Pena, A. M. et al. Three-dimensional investigation and scoring of extracellular matrix remodeling during lung fibrosis using multiphoton microscopy. *Microsc. Res. Tech.* **70**, 162–170 (2007).
35. Jos, *RANDBLOCK (10584)* (MATLAB Central File Exchange, accessed 28 May 2019); <https://www.mathworks.com/matlabcentral/fileexchange/17981-ranblock>
36. Desai, R. M., Koshy, S. T., Hilderbrand, S. A., Mooney, D. J. & Joshi, N. S. Versatile click alginate hydrogels crosslinked via tetrazine-norbornene chemistry. *Biomaterials* **50**, 30–37 (2015).
37. Chaudhuri, O. et al. Substrate stress relaxation regulates cell spreading. *Nat. Commun.* **6**, 6365 (2015).
38. Hosford, W. F. *Mechanical Behavior of Materials* (Cambridge Univ. Press, 2005).
39. Carr, D. A. & Peppas, N. A. Molecular structure of physiologically-responsive hydrogels controls diffusive behavior. *Macromol. Biosci.* **9**, 497–505 (2009).
40. Berger, J. et al. Structure and interactions in covalently and ionically crosslinked chitosan hydrogels for biomedical applications. *Eur. J. Pharm. Biopharm.* **57**, 19–34 (2004).
41. Boonthekul, T., Kong, H. J. & Mooney, D. J. Controlling alginate gel degradation utilizing partial oxidation and bimodal molecular weight distribution. *Biomaterials* **26**, 2455–2465 (2005).
42. Iza, M., Woerly, S., Danumah, C., Kaliaguine, S. & Bousmina, M. Determination of pore size distribution for mesoporous materials and polymeric gels by means of DSC measurements: thermoporometry. *Polymer* **41**, 5885–5893 (2000).
43. Backlund, M. P., Joyner, R. & Moerner, W. E. Chromosomal locus tracking with proper accounting of static and dynamic errors. *Phys. Rev. E* **91**, 062716 (2015).
44. Vorselen, D. et al. The fluid membrane determines mechanics of erythrocyte extracellular vesicles and is softened in hereditary spherocytosis. *Nat. Commun.* **9**, 4960 (2018).
45. Segur, J. B. & Oderstar, H. E. Viscosity of glycerol and its aqueous solutions. *Ind. Eng. Chem.* **43**, 2117–2120 (1951).
46. Calò, A. et al. Force measurements on natural membrane nanovesicles reveal a composition-independent, high Young's modulus. *Nanoscale* **6**, 2275–2285 (2014).

Acknowledgements

We thank B. Hoffman (Duke University) and L. Cai (University of Virginia) for critical reading of the manuscript and invaluable comments. We acknowledge P. Toth and the Core Imaging Facility at UIC, J. Li at the Department of Pharmacology at UIC, T. Foroozan at the UIC Nanotechnology Core Facility, T. Teng and J. Lee at the Department of Bioengineering at UIC, A. Song at UIC and the ANTEC facility at Northwestern University for their technical help and support. This work made use of instruments in the Fluorescence Imaging Core (Research Resources Center, UIC). This work was supported by National Institutes of Health Grant R01-HL141255 (J.-W.S.), R00-HL125884 (J.-W.S.), T32 HL07829 (S.L.) and American Heart Association Grant 19PRE34380087 (S.L.).

Author contributions

Conceptualization, S.L. and J.-W.S.; data curation, S.L.; formal analysis, S.L.; funding acquisition, S.L. and J.-W.S.; investigation, S.L., R.B. and G.C.; methodology, S.L. and J.-W.S.; project administration, S.L. and J.-W.S.; resources, J.-W.S.; software, S.L.; supervision, J.-W.S.; validation, S.L., R.B., G.C. and J.-W.S.; visualization, S.L.; writing original draft, S.L. and J.-W.S.; writing the revision, S.L. and J.-W.S.

Competing interests

The authors declare no competing interests.

Additional information

Supplementary information is available for this paper at <https://doi.org/10.1038/s41565-020-0636-2>.

Correspondence and requests for materials should be addressed to J.-W.S.

Peer review information *Nature Nanotechnology* thanks Gregor Fuhrmann, Neill Turner and the other, anonymous, reviewer(s) for their contribution to the peer review of this work.

Reprints and permissions information is available at www.nature.com/reprints.

Reporting Summary

Nature Research wishes to improve the reproducibility of the work that we publish. This form provides structure for consistency and transparency in reporting. For further information on Nature Research policies, see [Authors & Referees](#) and the [Editorial Policy Checklist](#).

Statistics

For all statistical analyses, confirm that the following items are present in the figure legend, table legend, main text, or Methods section.

n/a Confirmed

- ☐ ☒ The exact sample size (n) for each experimental group/condition, given as a discrete number and unit of measurement
- ☐ ☒ A statement on whether measurements were taken from distinct samples or whether the same sample was measured repeatedly
- ☐ ☒ The statistical test(s) used AND whether they are one- or two-sided
Only common tests should be described solely by name; describe more complex techniques in the Methods section.
- ☐ ☒ A description of all covariates tested
- ☐ ☒ A description of any assumptions or corrections, such as tests of normality and adjustment for multiple comparisons
- ☐ ☒ A full description of the statistical parameters including central tendency (e.g. means) or other basic estimates (e.g. regression coefficient) AND variation (e.g. standard deviation) or associated estimates of uncertainty (e.g. confidence intervals)
- ☐ ☒ For null hypothesis testing, the test statistic (e.g. F , t , r) with confidence intervals, effect sizes, degrees of freedom and P value noted
Give P values as exact values whenever suitable.
- ☒ ☐ For Bayesian analysis, information on the choice of priors and Markov chain Monte Carlo settings
- ☒ ☐ For hierarchical and complex designs, identification of the appropriate level for tests and full reporting of outcomes
- ☒ ☐ Estimates of effect sizes (e.g. Cohen's d , Pearson's r), indicating how they were calculated

Our web collection on [statistics for biologists](#) contains articles on many of the points above.

Software and code

Policy information about [availability of computer code](#)

Data collection

The following softwares were used to collect data in this study: IVIS Living Image 4.0 (PerkinElmer), Nanosight NTA 3.2 (Malvern), PrairieView 5.4 (Bruker), Rheocompass 1.24.584 (Anton Paar), AcquireSR 4.4 (GE), softWoRx 7.0.0 (GE), PHERAstar 3.0 (BMG LABTECH), QuantStudio 6/7 v1.3 (Applied Biosystems), IGOR Pro 6.3.7.2 (Wavemetrics), Asylum Research AFM Software 14.48.159 (Asylum Research), Advantage Software 5.5.24 (TA Instruments).

Data analysis

Prism 8 (GraphPad), ImageJ (NIH), IMARIS X64 9.3.0 (Bitplane) software and custom MATLAB 2019b scripts were used to analyze data in the study, as described fully in the methods section of the manuscript.

For manuscripts utilizing custom algorithms or software that are central to the research but not yet described in published literature, software must be made available to editors/reviewers. We strongly encourage code deposition in a community repository (e.g. GitHub). See the Nature Research [guidelines for submitting code & software](#) for further information.

Data

Policy information about [availability of data](#)

All manuscripts must include a [data availability statement](#). This statement should provide the following information, where applicable:

- Accession codes, unique identifiers, or web links for publicly available datasets
- A list of figures that have associated raw data
- A description of any restrictions on data availability

The datasets generated during and/or analysed during the current study are available from the corresponding author on reasonable request.

Field-specific reporting

Please select the one below that is the best fit for your research. If you are not sure, read the appropriate sections before making your selection.

☒ Life sciences ☐ Behavioural & social sciences ☐ Ecological, evolutionary & environmental sciences

For a reference copy of the document with all sections, see [nature.com/documents/nr-reporting-summary-flat.pdf](https://www.nature.com/documents/nr-reporting-summary-flat.pdf)

Life sciences study design

All studies must disclose on these points even when the disclosure is negative.

Sample size	Sample sizes were not predetermined based on statistical methods, but were chosen according to the standards of the field (at least three independent replicates for each condition). This provided a sufficient number of tracks for tracking data that allowed discussing the degree of differences between experimental groups. Specific details on sample size and statistical tests are provided in the manuscript.
Data exclusions	Tracking data were excluded as detailed in the methods section of the manuscript. Exclusion criteria was predefined based on previous studies: 1) Tracks with less than five measurements of mean squared displacement were excluded as noise, 2) Tracks with less than 20 measurements or greater than 30 measurements of mean squared displacement were excluded, as uneven track sizes can bias results.
Replication	All replication attempts were successful and included in the manuscript based on the sample size determination discussed above. Data in the main figures are presented as the mean +/- SEM of at least 3 independent replicates of the same experiment.
Randomization	Randomization was not relevant to the study since animals were not tested directly.
Blinding	Investigators were not blinded since experimental groups were easily identifiable by transport behaviors.

Reporting for specific materials, systems and methods

We require information from authors about some types of materials, experimental systems and methods used in many studies. Here, indicate whether each material, system or method listed is relevant to your study. If you are not sure if a list item applies to your research, read the appropriate section before selecting a response.

Materials & experimental systems

n/a	Involved in the study
<input type="checkbox"/>	<input checked="" type="checkbox"/> Antibodies
<input type="checkbox"/>	<input checked="" type="checkbox"/> Eukaryotic cell lines
<input checked="" type="checkbox"/>	<input type="checkbox"/> Palaeontology
<input type="checkbox"/>	<input checked="" type="checkbox"/> Animals and other organisms
<input checked="" type="checkbox"/>	<input type="checkbox"/> Human research participants
<input checked="" type="checkbox"/>	<input type="checkbox"/> Clinical data

Methods

n/a	Involved in the study
<input checked="" type="checkbox"/>	<input type="checkbox"/> ChIP-seq
<input checked="" type="checkbox"/>	<input type="checkbox"/> Flow cytometry
<input checked="" type="checkbox"/>	<input type="checkbox"/> MRI-based neuroimaging

Antibodies

Antibodies used	The primary antibodies used in this study were anti-AQP1 (SCBT, cat. no. sc-20810, clone no. H-55, lot no. 12005, dilution 1:2000) and anti-GAPDH (Proteintech, cat. no. 600004-1-Ig, clone no. 1E6D9, lot no. N/A, dilution 1:5000).
Validation	Each antibody has been validated previously by western blot to detect the indicated protein in mouse samples by over 15 independent studies, as indicated on the manufacturer's websites.

Eukaryotic cell lines

Policy information about [cell lines](#)

Cell line source(s)	The cell lines used in this study were D1 mouse MSCs (CRL-12424, ATCC), HeLa cells (CCL-2, ATCC), and HEK293T cells (CRL-3216, ATCC).
Authentication	No cell line was independently authenticated.
Mycoplasma contamination	Cells were tested for mycoplasma contamination and confirmed to be negative prior to conducting any experiment.
Commonly misidentified lines (See ICLAC register)	HeLa cells and HEK293T cells used in this study were of low passage number directly from an authentic stock obtained from the supplier.

Animals and other organisms

Policy information about [studies involving animals](#); [ARRIVE guidelines](#) recommended for reporting animal research

Laboratory animals	10 week old female C57BL/6J mice were used in this study.
Wild animals	The study did not involve wild animals.
Field-collected samples	The study did not involve samples collected from the field.
Ethics oversight	All animal procedures were performed in compliance with NIH, AAALAC, and institutional guidelines approved by the ethical committee from the University of Illinois at Chicago.

Note that full information on the approval of the study protocol must also be provided in the manuscript.

In the format provided by the authors and unedited.

Matrix mechanics and water permeation regulate extracellular vesicle transport

Stephen Lenzini, Raymond Bargi, Gina Chung and Jae-Won Shin  *

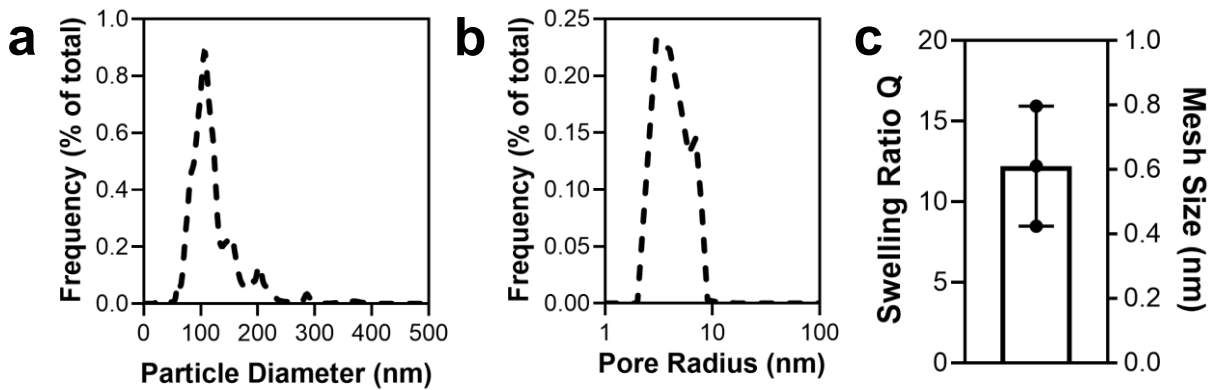
Department of Pharmacology and Department of Bioengineering, University of Illinois at Chicago, Chicago, IL, USA. *e-mail: shinwj@uic.edu

Supplementary Information

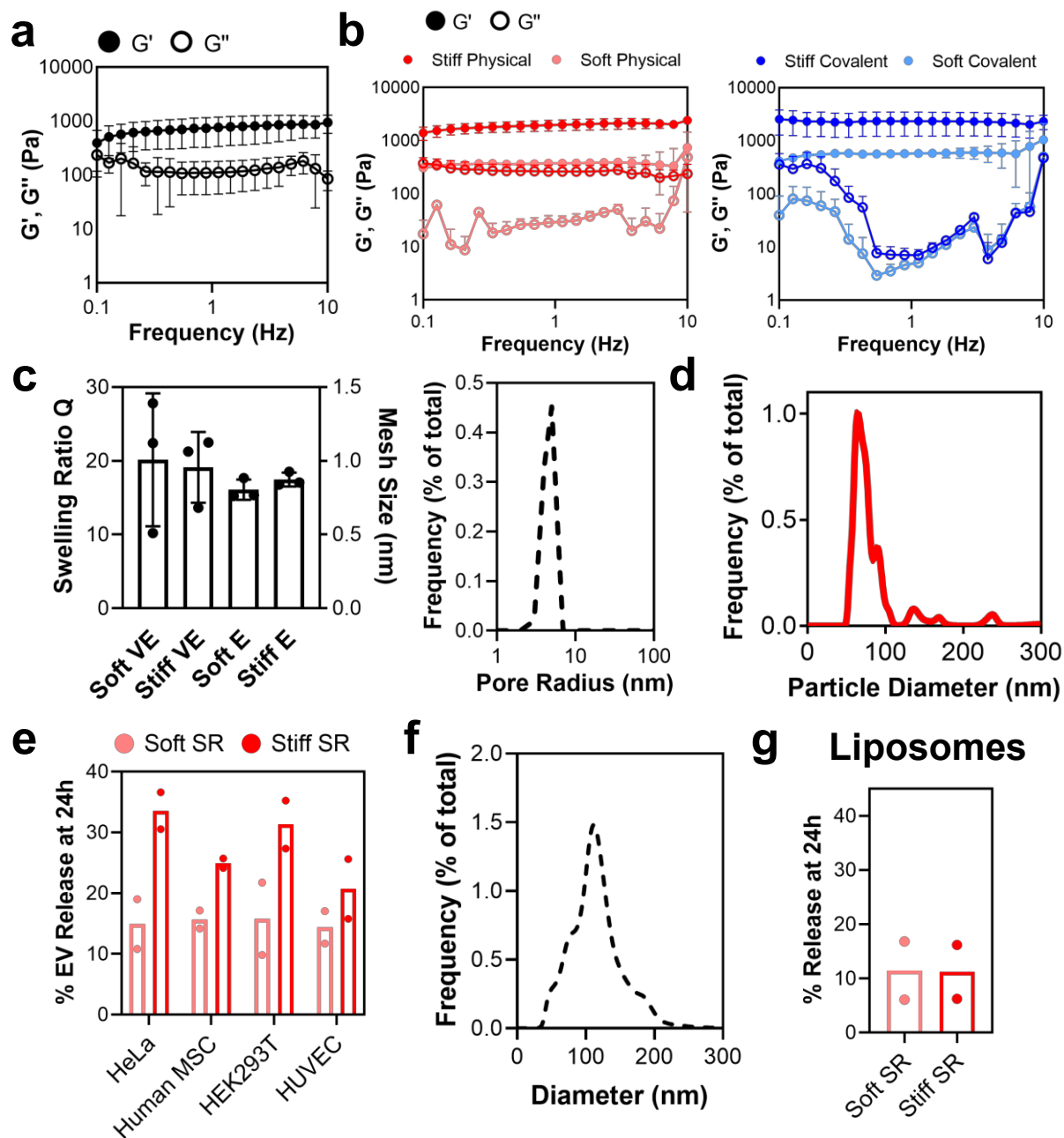
Title: Matrix mechanics and water permeation regulate extracellular vesicle transport

Authors: Stephen Lenzini¹, Raymond Bargi¹, Gina Chung¹, Jae-Won Shin^{1*}

Supplementary Figures

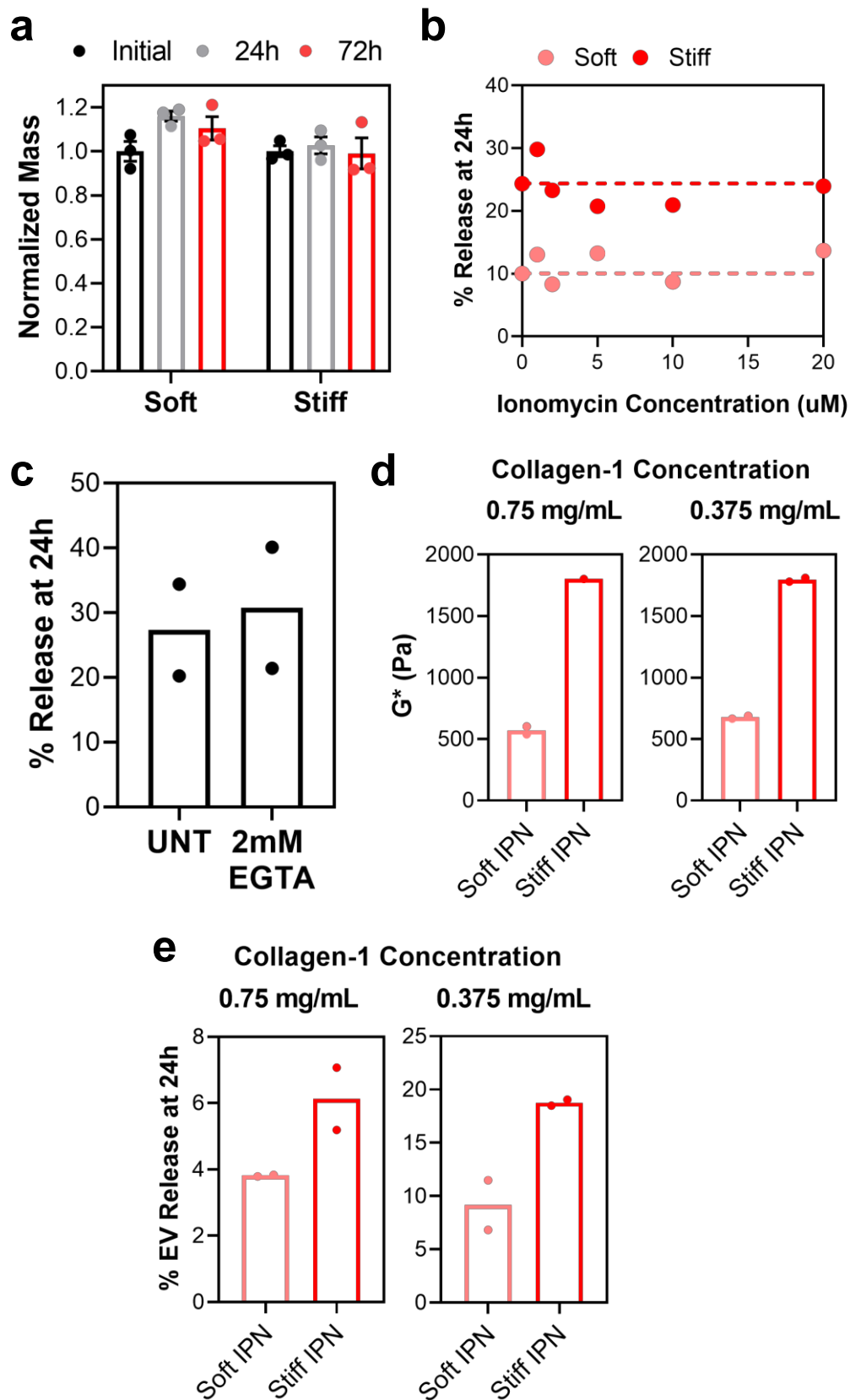


Supplementary Fig. 1. Relative sizes of EVs and decellularized lung ECM mesh. a, Representative EV size distribution. Data represents the mean of $N = 3$ preparations. **b,** Pore size distribution of decellularized lung tissue as measured by differential scanning calorimetry for $N = 1$ tissue slice. **c,** Mean mesh size as calculated by equilibrium swelling theory for $N = 3$ tissue slices over 2 independent experiments. Error bars are SD.

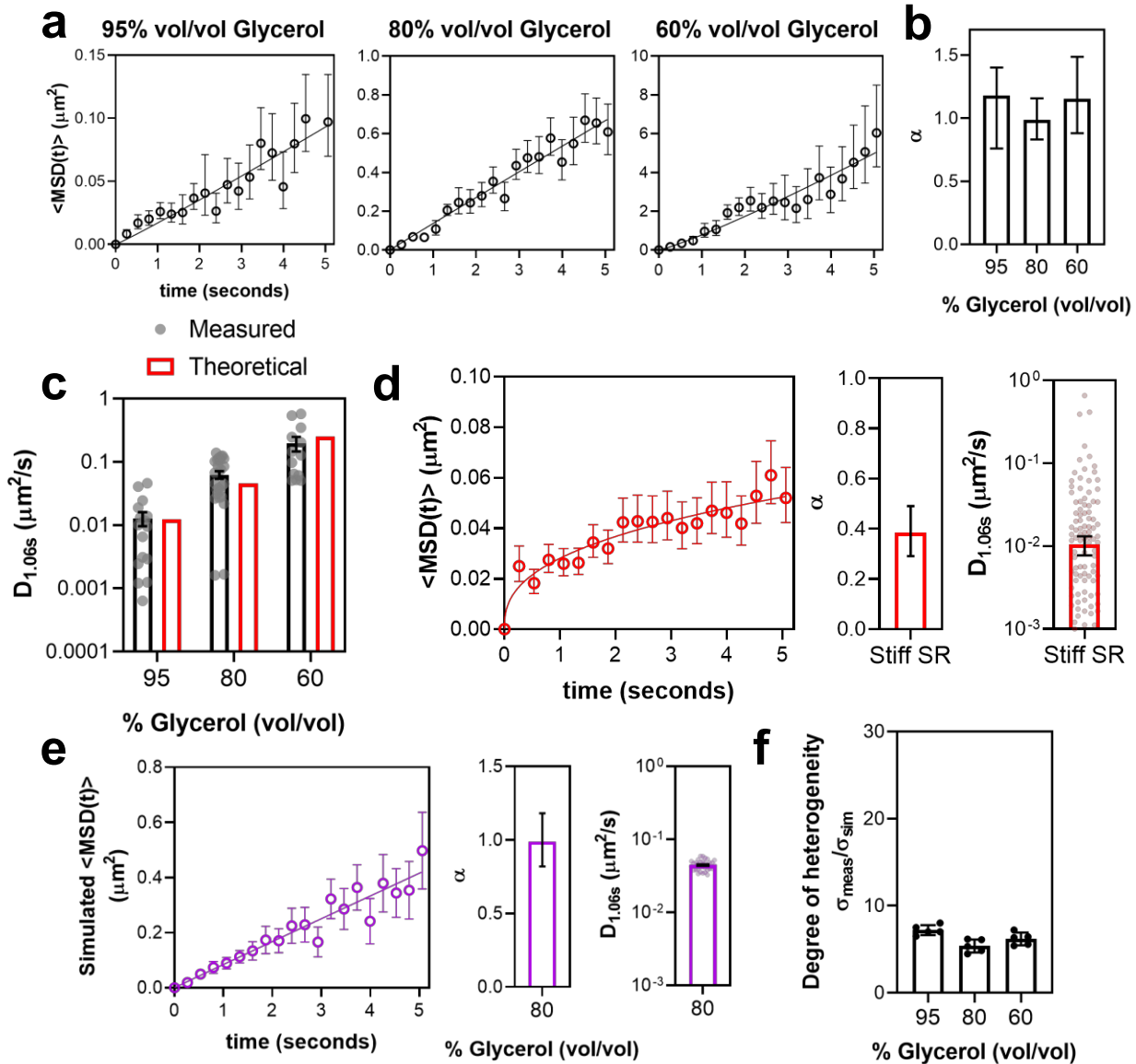


Supplementary Fig. 2. Physical properties of tissue ECM and engineered hydrogels with their effect on particle release. **a**, Frequency sweep of storage and loss moduli for decellularized lung tissue. $N = 3$ tissue slices. **b**, Frequency sweep of storage and loss moduli for hydrogels. (Left) Physically crosslinked stress relaxing hydrogels. (Right) Covalently crosslinked elastic hydrogels. $N = 3$ hydrogels for each condition. **c**, Hydrogel mesh size

calculations. (Left) Calculated by equilibrium swelling theory, $N = 3$ hydrogels for each condition. (Right) Calculated by differential scanning calorimetry for stiff stress relaxing hydrogel, $N = 1$ hydrogel. **d**, Representative NP size distribution. $N = 3$ preparations. **e**, EVs derived from multiple cell types exhibit increased release from stiffer versus softer stress relaxing hydrogels. Each $N = 2$ hydrogels. **f**, Size distribution of liposomes with similar lipid composition to EVs. $N = 1$ preparation. **g**, Liposomes do not exhibit increased release from stiffer versus softer stress relaxing hydrogels. $N = 2$ hydrogels. Unless stated otherwise, data are obtained across $= 3$ independent experiments and error bars denote SEM.

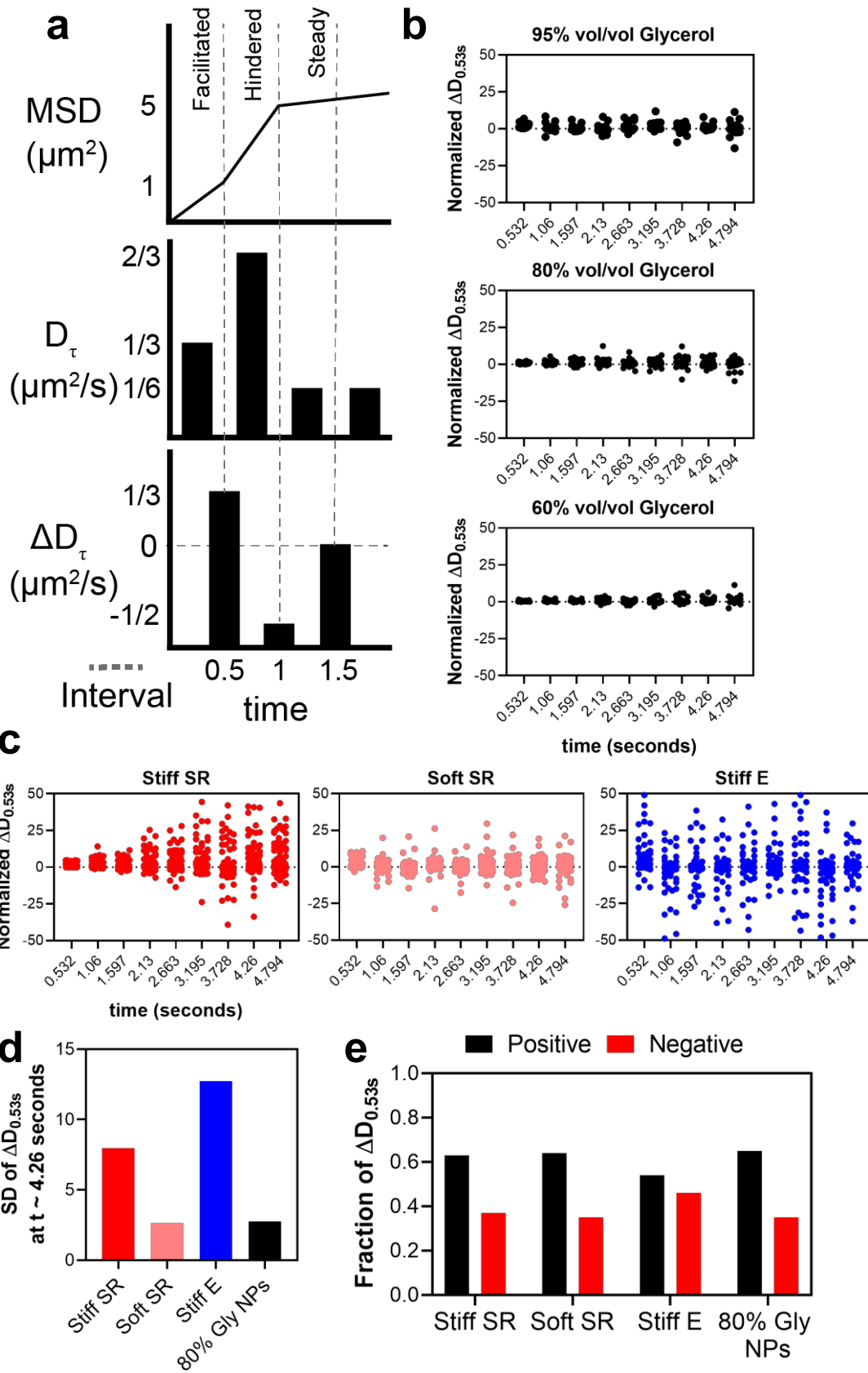


Supplementary Fig. 3. Examination of increased EV release from hydrogels. **a**, Stress relaxing hydrogels do not lose mass over the tested time period. Mass is normalized to hydrogel initial mass after 1 hour. Data represents the mean of $N = 3$ hydrogels across one experiment. **b**, Treatment of EVs encapsulated in hydrogels with ionomycin, a compound that facilitates calcium flux across membranes, does not affect EV release across a range of ionomycin concentrations. Dotted lines represent 0 mM ionomycin. $N = 2$ hydrogels across 2 independent experiments. **c**, Treatment of hydrogels with 2 mM EGTA, a calcium chelator, does not affect EV release. Data represents the mean of $N = 2$ hydrogels within one experiment. **d**, Interpenetrating network (IPN) hydrogels of collagen-1 and alginate exhibit tunable G^* independent of collagen-1 concentration. Data represents the mean of $N = 2$ hydrogels for each condition. **e**, Though EVs release less overall with increasing collagen-1 concentration, release is greater from stiffer versus softer IPN hydrogels. $N = 2$ hydrogels for each condition. Unless stated otherwise, error bars denote SD.

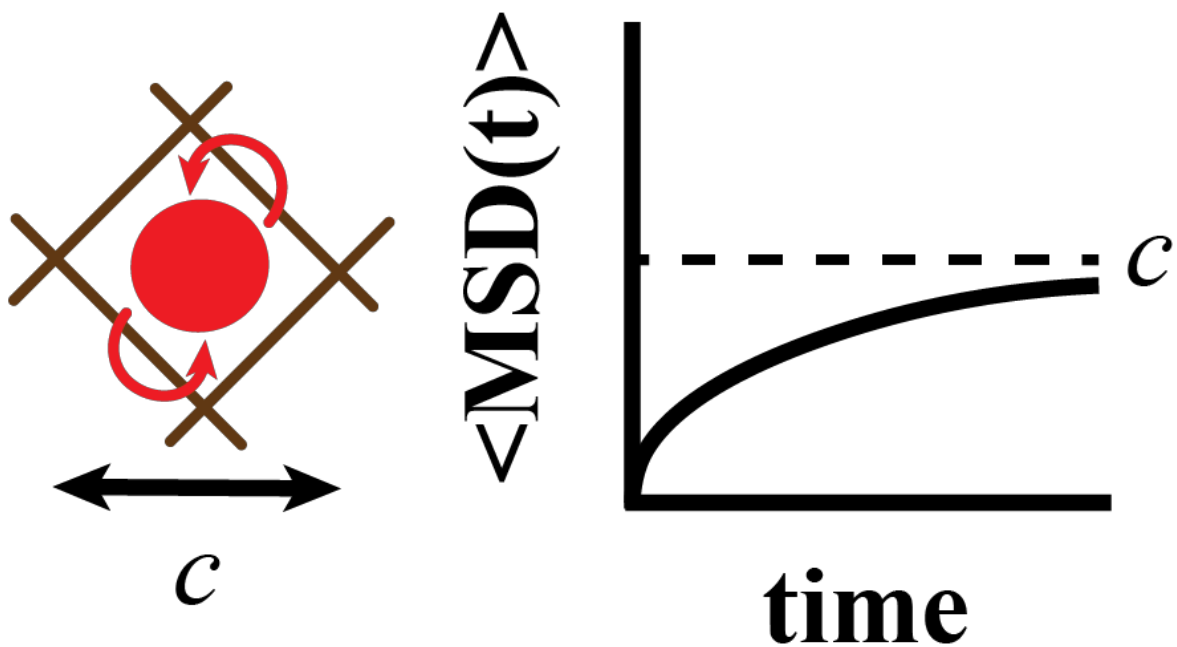


Supplementary Fig. 4. Validation of 3D particle tracking methods using nanoparticles. **a**, Ensemble MSD curves for polystyrene nanoparticles transporting in solutions with various amounts of glycerol: 95% ($N = 17$), 80% ($N = 32$), 60% ($N = 13$). **b**, Values for effective transport exponent α by a non-linear fit of Equation 1 for curves presented in (a). Values are close to 1 as expected for particles transporting freely in solution. Error bars are 95% CI. **c**, Mean diffusion coefficient $D_{1.06s}$ for nanoparticles transporting in each solution of glycerol matches that expected based on the theoretical Stokes-Einstein relationship. **d**, (Left) Ensemble MSD

curves for polystyrene nanoparticles transporting in stiff stress relaxing matrix. (Middle) The value of α for nanoparticles in matrix is less than 1, indicating sub-diffusion. Error bars are 95% CI. (Right) Mean diffusion coefficient $D_{1.06s}$ for nanoparticles in matrix. Data are for $N = 343$ tracks. **e**, (Left) Simulated *MSD* curve for nanoparticles transporting in 80% vol/vol glycerol solution with (Middle) α value and (Right) $D_{1.06s}$. The curve and the values are similar to (b, Middle) as expected. $N = 32$ tracks. Error bars denote 95% CI. **f**, Degree of heterogeneity $\sigma_{meas}/\sigma_{sim}$ for nanoparticles transporting in glycerol solutions. $N = 5$ simulations. Error bars denote SEM.

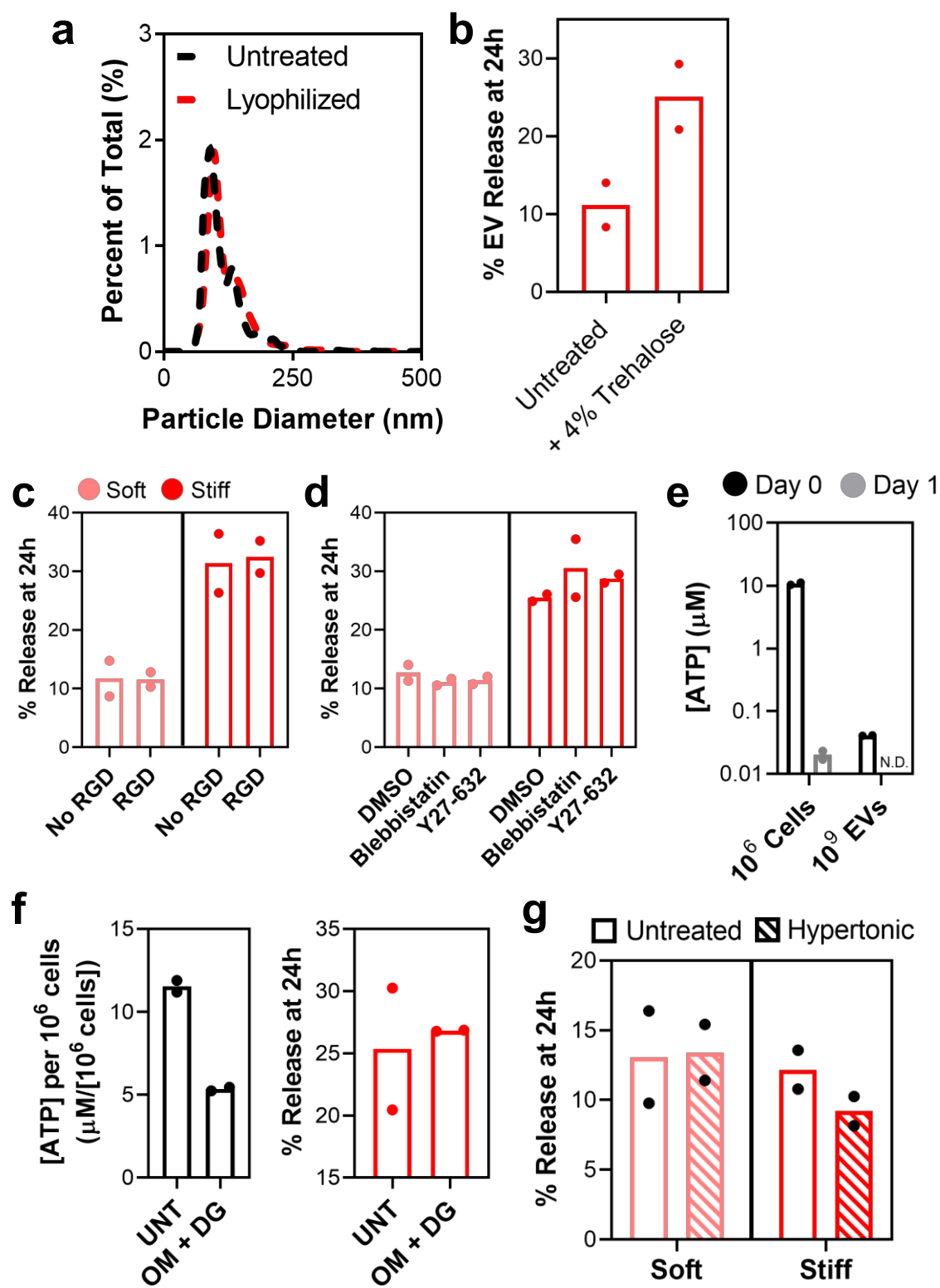


Supplementary Fig. 5. Analysis of EV tracking data. **a**, Illustration of the relationship between $MSD(t)$, D_τ , and ΔD_τ values. Particle motion remains constant when $\Delta D_\tau \sim 0$, particle motion is facilitated when $\Delta D_\tau > 0$, and particle motion is hindered when $\Delta D_\tau < 0$. Values are arbitrary and for illustrative purposes only. **b**, Values for $\Delta D_{0.53s}$ over the length of the track for nanoparticles transporting in glycerol, 95% ($N = 17$), 80% ($N = 32$), 60% ($N = 13$). **c**, Values for $\Delta D_{0.53s}$ over the length of the track for EVs transporting in matrix, Stiff SR ($N = 279$), Soft SR ($N = 263$), Stiff E ($N = 89$). **d**, Standard deviation (SD) of $\Delta D_{0.53s}$ distributions for tracks in Fig. 3b measured at $t \sim 4.26$ seconds. **e**, Fraction of all $\Delta D_{0.53s}$ values for particle tracks with positive or negative value.



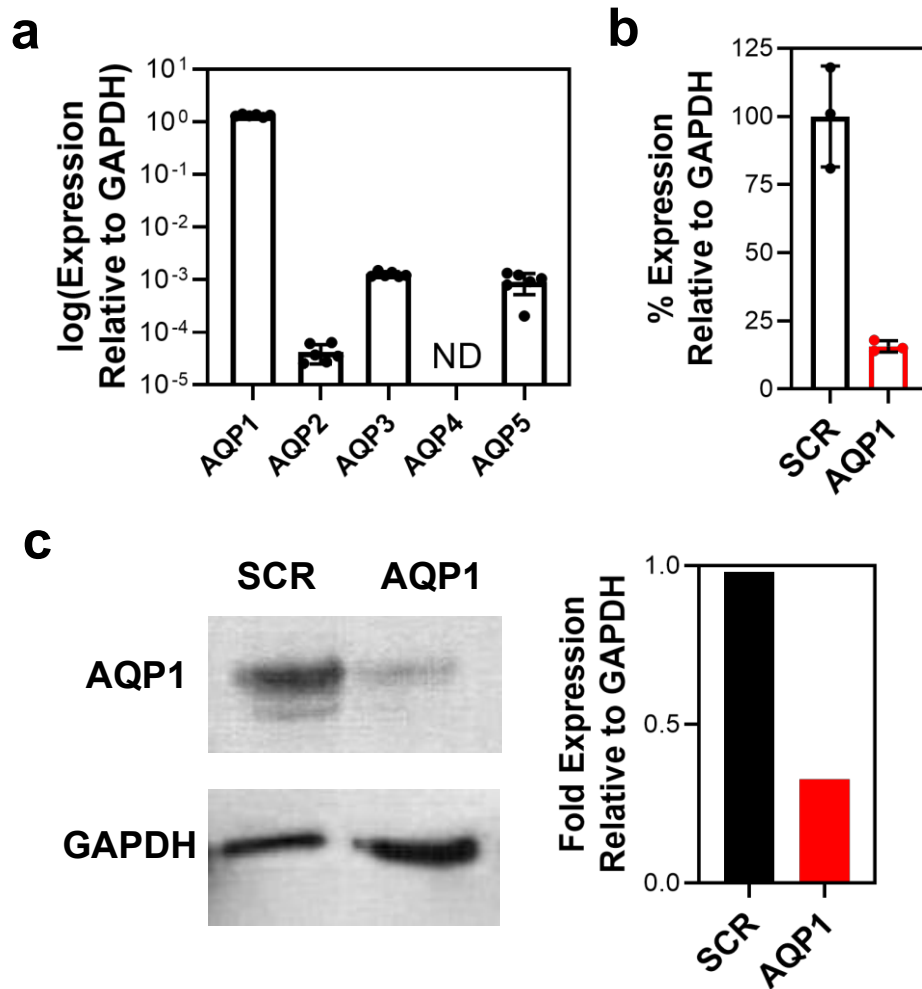
Supplementary Fig. 6. Illustration of cage size determined for nanoparticles in matrix.

Particles under confinement in matrix exhibit an *MSD* that can be used to model the system as a set of cages with size c defined by the *MSD* plateau.



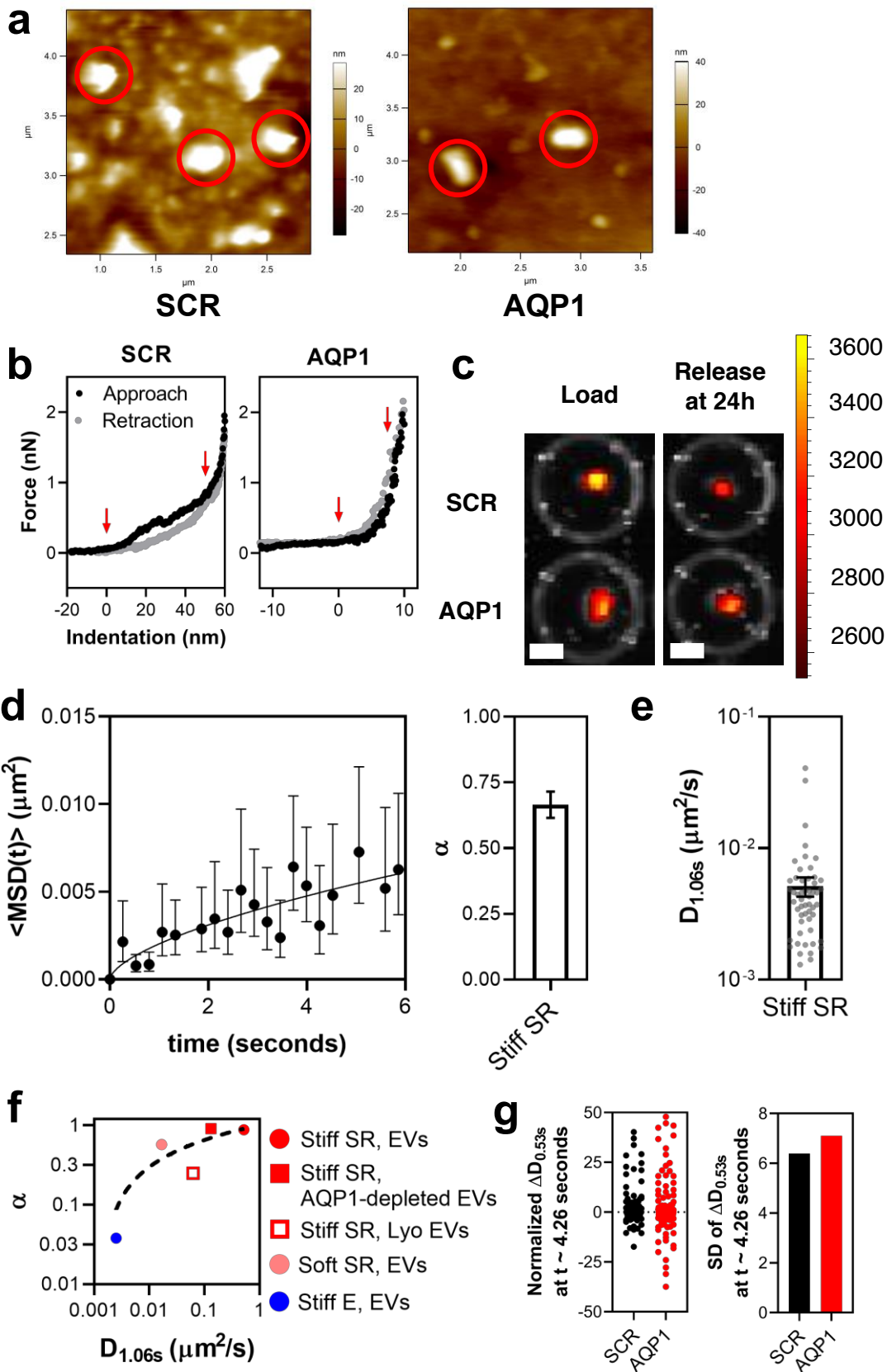
Supplementary Fig. 7. Mechanisms of mechanosensitive EV release from hydrogels. a,

Lyophilization of EVs does not affect their size distribution after reconstitution. $N = 2$ preparations. **b,** Addition of 4% trehalose to EVs during lyophilization recovers their mean % release in stiff stress relaxing matrix. $N = 2$ hydrogels each condition. **c,** Presence of $0.8 \mu\text{M}$ RGD peptide tethered within stress relaxing hydrogels does not affect mean % EV release. **d,** Treating RGD-hydrogels containing encapsulated EVs with cytoskeletal inhibitors does not affect mean % EV release. **e,** EVs contain little ATP in comparison to their cells. The 10^9 EVs are isolated from the 10^6 cells over 24 hours. $N = 2$ preparations within one experiment. **f,** (Left) Cells are depleted of ATP by $\sim 50\%$ with treatment with $1 \mu\text{g/mL}$ oligomycin (OM) and 1mM 2-deoxy-D-glucose (DG). (Right) EVs from cells depleted of ATP do not exhibit a different release after 24 hours from stiff stress relaxing hydrogels. $N = 2$ hydrogels for each condition. **g,** Treating lyophilized EVs encapsulated in stress relaxing hydrogels with hypertonic solution does not affect their mean % release. Unless stated otherwise, all release experiments represent $N = 2$ hydrogels across 2 independent experiments and error bars denote SD.



Supplementary Fig. 8. Aquaporin-1 knockdown in EVs.

a, *AQP1* is the dominant aquaporin isoform in mMSCs. The y-axis is expressed as the log fold change of RNA expression relative to *GAPDH* RNA expression. Data represent the mean of $N = 3$ reactions in one experiment. **b**, Verification of RNA expression knockdown in cells by treatment with siRNA against *AQP1*. SCR = scrambled siRNA control. Data represent $N = 3$ reactions in one experiment. **c**, EVs collected from cells treated with siRNA against *AQP1* express less AQP1 protein. (Left) Western blot of EVs from cells treated with siRNA against *AQP1* or a scrambled (SCR) control siRNA. (Right) Blot quantification.



Supplementary Fig. 9. Effect of aquaporin-1 knockdown in EVs.

a, Representative images of EVs adhered to mica acquired using scanning mode with atomic force microscopy. Red circles indicate particles measuring 50-150nm in height that are measured for Young's modulus. **b**, Representative force-displacement curves of EVs from cells treated with siRNA against *AQP1* versus a control. Red arrows indicate the range in which Young's modulus is calculated. **c**, Representative image of AQP1-depleted EVs largely remaining within decellularized lung tissue 24 hours after loading. The axis scale is fluorescence intensity counts (AU). Scale bars = 2 mm. **d**, (Left) Ensemble *MSD* curves for liposomes in stiff stress relaxing matrix. (Right) Value for transport exponent α for the *MSD* curve. Error bars denote 95% CI. Data are for $N = 58$ tracks. **e**, Mean diffusion coefficient $D_{1.06s}$ for liposomes in stiff stress relaxing matrix from (d). **f**, Values for α and mean $D_{1.06s}$ plot for all groups of EVs in matrix measured in this study fit to a standard one-phase association curve. **g**, Distributions of the change in local transport coefficient $\Delta D_{0.53s}$ calculated at time ~ 4.26 seconds are similar for AQP1-depleted EVs ($N = 613$) versus a control ($N = 659$). Particles are analysed for $N \geq 180$ tracks for each condition. Unless stated otherwise, error bars denote SEM.

Supplementary Movies

Movie S1: Tracking data overlaid with imaging data for representative transport of a single EV in stiff stress relaxing matrix shown in Fig. 3A. The length scale is micrometers and the time scale is seconds.

Movie S2: Tracking data overlaid with imaging data for representative transport of a single EV in soft stress relaxing matrix shown in Fig. 3A. The length scale is micrometers and the time scale is seconds.

Movie S3: Tracking data overlaid with imaging data for representative transport of a single EV in stiff elastic matrix shown in Fig. 3A. The length scale is micrometers and the time scale is seconds.

Movie S4: Tracking data overlaid with imaging data for representative transport of multiple EVs in stiff stress relaxing matrix. The length scale is micrometers and the time scale is seconds.

Movie S5: Tracking data overlaid with imaging data for representative transport of multiple EVs in soft stress relaxing matrix. The length scale is micrometers and the time scale is seconds.

Movie S6: Tracking data overlaid with imaging data for representative transport of multiple EVs in stiff elastic matrix. The length scale is micrometers and the time scale is seconds.

Supplementary Table 1. Quantitative PCR primers.

Target	Sequence
<i>GAPDH</i>	F: ACATCGCTCAGACACCATG R: TGTAGTTGAGGTCAATGAAGGG
<i>AQP1</i>	F: CTGGCGATTGACTACACTGG R: AAGTCATAGATGAGCACTGCC
<i>AQP2</i>	F: TTGGTTTCTCTGTTACCCTGG R: AACGGGCTGGATTCATGG
<i>AQP3</i>	F: CTTTGCCACCTATCCCTCTG R: CCACAGTGAAAGCCTCCAG
<i>AQP4</i>	F: GCTTAGATCTGGCTTTCAAAGG R: AATGTCCACACTTACCCAC
<i>AQP5</i>	F: CTCCCCAGCCTTATCCATTG R: ACCCAGAAGACCCAGTGAG